RSC Advances

PAPER

View Article Online
View Journal | View Issue

Cite this: *RSC Adv.*, 2025, **15**, 42740

Sparse silver loading on chitosan–boron carbon nitride framework: a sustainable route to multifunctional nanomaterials

Aakhila Banu, [a] C. V. Yelamaggad[b] and Siddappa A. Patil *[a]

The design of multifunctional nanomaterials capable of addressing both environmental and biomedical challenges is a growing focus in modern materials science. In this study, we report the synthesis of a silver nanoparticle-embedded on chitosan–boron carbon nitride (Ag@CS–BCN), crosslinked with glutaraldehyde, *via* a multi-step process. The structural, morphological, elemental, and stability characteristics of the synthesised nanohybrid systematically investigated using spectroscopic and microscopic techniques. The catalytic performance of Ag@CS–BCN was evaluated for the reduction of 4-nitrophenol (4-NP) and the degradation of methyl orange (MO) and rhodamine B (RhB), persistent organic pollutants of environmental concern. The nanocomposite exhibited rapid catalytic activity, achieving >94% degradation within minutes (4-NP: 5 min, 99.82%; MO: 3 min, 94.50%; RhB: 7 min, 98.89%), and demonstrated recyclability for up to three consecutive cycles with minimal loss in performance. Beyond environmental applications, Ag@CS–BCN displayed potent antimicrobial efficacy against both Gram-positive and Gram-negative bacterial strains. Importantly, cytotoxicity studies revealed selective anticancer activity, with an IC_{50} value of 45.73 μg mL^{-1} against HeLa cancer cells and substantially lower toxicity toward normal 3T3 fibroblasts (IC_{50} = 446.6 μg mL^{-1}). Overall, the Ag@CS–BCN nanohybrid demonstrates significant promise as a multiple-purpose material for environmental remediation and biomedical applications, particularly in nanocatalysis, antimicrobial, and targeted anticancer therapy, thereby offering an innovative platform for sustainable and therapeutic technologies.

Received 22nd September 2025
Accepted 24th October 2025

DOI: 10.1039/d5ra07185b

rsc.li/rsc-advances

1. Introduction

Industrialisation and urbanisation have significantly contributed to environmental pollution by the extensive release of organic dyes and nitroaromatic compounds into water bodies.[1–3] These pollutants, which include hazardous dyes such as methyl orange (MO), rhodamine B (RhB), and nitroarene derivatives, are persistent, non-biodegradable, and toxic to aquatic life and humans.[1,4,5] Nitroarenes are particularly alarming due to their high electron-withdrawing nitro groups, which make them chemically stable and resistant to degradation.[6] Prolonged exposure to nitroarenes has been associated with genotoxicity, mutagenicity, and carcinogenic effects, especially through contamination of drinking water sources.[7,8] They can interfere with cellular respiration, induce oxidative stress, and adversely affect the human liver and central nervous system.[8] In industrial settings, the uncontrolled discharge of nitroarenes has been linked to severe groundwater and soil contamination, resulting in long-term ecological imbalance.[9]

Similarly, synthetic dyes such as MO and RhB, extensively used in the textile, cosmetic, and food industries, pose a major risk when released untreated into the environment.[1] Methyl orange, an azo dye, and rhodamine B are classified as potential carcinogens and mutagens. They cause long-term ecological damage by blocking sunlight penetration in aquatic ecosystems, thereby reducing photosynthetic activity.[1,10] Their bioaccumulation in marine organisms also threatens the food chain. In humans, exposure through contaminated water can result in skin irritation, respiratory distress, and damage to internal organs.[11] These dyes persist in the environment due to their complex aromatic structures and high chemical stability, making their removal from wastewater a critical objective in environmental science.[12] In recent reports, MO has been found to induce cytotoxic and haematological abnormalities in animal models, while RhB has been implicated in neurotoxicity and reproductive toxicity, leading to growing regulatory concerns in many countries.[13,14] Their reduction to less toxic or biodegradable forms is crucial for detoxification and converting valuable amine derivatives, which serve as valuable intermediates in the pharmaceutical and chemical industries. Sodium borohydride ($NaBH_4$) is a commonly employed reducing agent due to its

[a]*Centre for Nano and Material Sciences, Jain (Deemed-to-be University), Jain Global Campus, Kanakapura, Bangalore, Karnataka, India-562112. E-mail: p.siddappa@jainuniversity.ac.in; patilsiddappa@gmail.com*

[b]*Centre for Nano and Soft Matter Sciences, Survey No. 7, Shivanapura, Bangalore, 562162, India*

stability in aqueous media, high reducing potential and less harmful byproducts.[15] However, its efficiency for nitroarene and dye reduction is often limited without a suitable catalyst, necessitating the development of nanostructured catalysts that can mediate fast electron transfer to accelerate the reaction kinetics.[16] Simultaneously, the degradation of organic dyes like MO and RhB dyes remains a priority for environmental remediation. Catalytic degradation, especially through photocatalysis and redox-mediated pathways, has emerged as an effective strategy.[17] The application of multifunctional nanomaterials that can catalyse both nitroarene reduction and dye degradation offers a sustainable approach and allows the exploration of additional biomedical properties, such as antimicrobial and anticancer activities. Recent studies have highlighted a compelling link between catalytic activity and biological efficacy. For instance, nanoparticles capable of electron mediation in chemical reactions often generate reactive oxygen species (ROS) under biological conditions, contributing to antimicrobial efficacy by damaging microbial membranes and DNA.[18] Similarly, the redox potential that enables dye degradation and nitroarene reduction can also induce oxidative stress in cancer cells, leading to apoptosis.[19,20] This dual activity provides a platform for designing nanomaterials that are both environmentally and biomedically relevant.

Nanohybrid is a class of nanomaterials which combines both organic and inorganic constituents intricately assembled through non-covalent interactions, resulting in multifunctional architectures with tailored properties. These nanohybrids are not simple physical mixtures. They are generally characterised as nanocomposites comprising intimately integrated organic/inorganic constituents. Their modular structure enables the integration of biocompatibility, functional responsiveness, and stability. Their structural diversity and interfacial tunability make them ideal for next-generation material design.[21,22]

Among various nanomaterials, silver nanoparticles (AgNPs) have gained immense attention due to their unique physicochemical properties, including surface plasmon resonance, high surface-to-volume ratio, and ease of functionalization.[23,24] AgNPs are well-known for their antimicrobial potency against a broad spectrum of pathogens and exhibit cytotoxic effects on a variety of cancer cell lines.[25] Their antimicrobial action is often attributed to the generation of ROS, release of Ag^+ ions, and disruption of membrane integrity. Moreover, AgNPs have been explored in catalysis for their ability to facilitate electron transfer reactions, making them ideal candidates for dye degradation and nitroarene reduction.[26,27]

They are often incorporated into natural polymeric matrices to enhance the stability, biocompatibility, and catalytic activity of AgNPs. Chitosan, a biodegradable and biocompatible polysaccharide derived from chitin, is one such matrix. It possesses intrinsic antimicrobial properties and can stabilise nanoparticles through electrostatic interactions.[28] Crosslinking chitosan with glutaraldehyde improves its mechanical strength and water stability, thereby enhancing its applicability in aqueous environments.[29] Furthermore, the integration of boron carbon nitride (BCN), a two-dimensional layered material with high chemical stability and surface activity, offers additional advantages. BCN serves as a robust support matrix that facilitates uniform nanoparticle dispersion and increases surface active sites, thereby improving catalytic and biological performance.

Additionally, the antimicrobial mechanism of such composites is multifaceted, involving both direct contact killing through membrane disruption and indirect oxidative stress pathways. These materials are effective against Gram-positive and Gram-negative bacteria, as well as fungal strains. Their anticancer potential is equally promising, with reports indicating effective inhibition of cell proliferation, induction of apoptosis, and interference with cell cycle progression in various human cancer cell lines. The integration of catalysis and biomedicine offers a novel route for the development of theranostic agents. Materials capable of degrading environmental pollutants and simultaneously exerting antimicrobial and anticancer effects represent a new generation of functional nanomaterials that align with the principles of green chemistry and sustainable development.

In this study, we aimed to extend the application of AgNPs-based nanohybrid in wastewater treatment, followed by antimicrobial and anticancer activity by synthesising an inert and efficient chitosan crosslinked with glutaraldehyde and BCN onto which AgNPs were immobilised *via* a straightforward multi-step protocol. The resulting low-loaded nanohybrid, denoted as Ag@CS–BCN, was thoroughly characterised to determine its structural and compositional features. Its catalytic performance was then evaluated through the reduction and degradation of nitroarenes and MO and RhB dyes using $NaBH_4$ as the reducing agent. Furthermore, antimicrobial and anticancer activities of Ag@CS–BCN were investigated, highlighting their dual functionalities in environmental remediation and biomedical applications.

2. Experimental

2.1. Materials

Melamine, boric acid, chitosan, glacial acetic acid, silver nitrate ($AgNO_3$), sodium borohydride ($NaBH_4$), sodium hydroxide (NaOH) pellets, methanol, ascorbic acid, 4-nitrophenol, nitroarenes, MO, RhB, and glutaraldehyde solution (25%) were purchased from Merck, Sigma-Aldrich, SDFCL, and Avra Chemical Companies, India. All chemicals used in this study were of high-purity analytical grade and were employed without any additional purification. Bacterial strains such as *Escherichia coli*-44 and *Staphylococcus aureus*-902 were obtained from the Microbial Type Culture Collection (MTCC), Chandigarh, India. Nutrient agar, nutrient broth, and gentamicin solution were procured from Hi-Media Laboratories, India. For antifungal studies, potato dextrose agar (PDA) medium and amphotericin B were used. All microbiological consumables, such as Petri plates, test tubes, conical flasks, and beakers, were supplied by Borosil, India. Double-distilled water was used for all experimental procedures. Fetal Bovine Serum (FBS), antibiotic–antimycotic solution, and Dulbecco's Modified Eagle Medium (DMEM) were purchased from Gibco (USA). Dimethyl sulfoxide (DMSO) and MTT (3-(4,5-dimethylthiazol-2-yl)-2,5-

diphenyltetrazolium bromide).[30] were obtained from Sigma-Aldrich (USA). Phosphate-buffered saline (1× PBS) was sourced from Indian Vendors. Tissue culture consumables, including 96-well plates and wash beakers, were supplied by Tarsons, India. Mouse fibroblast (3T3) and human cervical cancer (HeLa) cell lines were sourced from the National Centre for Cell Science (NCCS), Pune, India. All reactions were performed under ambient conditions unless stated otherwise.

2.2. Instrumentation and analyses

FT-IR spectroscopy was carried out using a PerkinElmer Spectrum Two spectrometer. The crystal structure and diffraction pattern were analysed *via* powder X-ray diffraction (*p*-XRD) using a Rigaku Ultima-IV diffractometer. Morphological features and elemental composition were examined separately using field emission scanning electron microscopy (FE-SEM) and energy dispersive X-ray spectroscopy (EDS) with a JEOL JSM7100F. X-ray photoelectron spectroscopy (XPS) analyses were performed using a Thermofisher Nexsa XPS instrument with an Al Kα X-ray source (vacuum: 10^{-8} mbar, pass energy: 200 eV, dwell time: 10 ms, binding energy scale: 0–1350). Transmission electron microscopy (TEM) images were acquired using a JEOL JEM-2100 microscope. HR-TEM imaging was conducted using a JEOL JEM-2100 microscope. The surface area was measured using nitrogen adsorption–desorption analysis based on the Brunauer–Emmett–Teller (BET) method executed on a Microtrac BELSORP MAX instrument. Thermogravimetric (TG) analysis was carried out using a PerkinElmer STA 6000 TG/DTA in a nitrogen atmosphere, covering a temperature range of 50 to 900 °C at a heating rate of 10.0 °C min^{-1}. The catalytic activity of the synthesised Ag@CS–BCN nanohybrid was examined using a UV-visible spectrophotometer (UV-1900i, Shimadzu, Japan).

2.3. Synthesis of boron carbon nitride (BCN)

Melamine powder (12 g) and boric acid (6 g) were mixed in a 2 : 1 ratio using a mortar and pestle for 15 min. The mixture was then transferred to a crucible and calcined at 500 °C for 4 h. After cooling to room temperature, 6.52 g of yellow boron carbon nitride (BCN) powder was obtained and stored in a transparent vial at ambient temperature for further use. This method is consistent with previously reported literature.[31]

2.4. Synthesis of silver nanoparticles anchored on boron carbon nitride and cross-linked chitosan with glutaraldehyde (Ag@CS–BCN)

Chitosan powder (2 g) was first dissolved in 200 mL of 2% (v/v) glacial acetic acid under constant stirring to prepare a clear chitosan solution. To this, an appropriate amount of BCN powder and 1 mL of 25% glutaraldehyde were added as the crosslinking agent. Subsequently, silver nitrate ($AgNO_3$) was dispersed at a concentration of 1.76 wt%, followed by the addition of ascorbic acid (0.0352 g) as a reducing agent. After an additional 2 hours of stirring, the colour transitioned from yellow to fern green. To facilitate precipitation, NaOH (1 M) was dissolved in a methanol: water mixture (1 : 1 v/v) and added dropwise. The resulting nanohybrid material, Ag@CS–BCN, was thoroughly washed with distilled water several times until a neutral pH was achieved. These parameters were carefully chosen to ensure the complete solubilization of chitosan while minimising the acid-catalysed degradation. Literature reports have shown that excessive exposure to an acidic environment can lead to chain scission and the formation of low-molecular-weight oligomers, which may negatively impact the structural integrity of the framework.[32,33] It was then dried in a hot air oven at 50 °C for 24 h. A final yield of 5.05 g of fern green-coloured Ag@CS–BCN nanohybrid was obtained and stored in an airtight vial at room temperature for further characterisation and applications.

2.5. General procedure for the reduction of nitroarenes using Ag@CS–BCN nanohybrid as a nanocatalyst

A freshly prepared aqueous solution of $NaBH_4$ (0.4 M, 10 mL) was mixed with an aqueous solution of nitroarenes (2.5 mM, 10 mL) under gentle stirring. To this reaction mixture, Ag@CS–BCN (0.08 mol%) nanohybrid was added. The progress of the reduction reaction was monitored by observing changes in UV-visible absorbance at specific time intervals. At the desired time, an aliquot of the reaction mixture was withdrawn, diluted with distilled water, and analysed to assess the extent of reduction. Once the reaction was complete, the Ag@CS–BCN nanohybrid was separated by centrifugation.

2.6. General procedure for the degradation of MO using Ag@CS–BCN nanohybrid as a nanocatalyst

The Ag@CS–BCN (0.08 mol%) nanohybrid was added to the aqueous solution of MO (0.2 mM, 25 mL) under mild stirring. Subsequently, a freshly prepared aqueous solution of $NaBH_4$ (0.45 M, 10 mL) was added to the reaction mixture. The reduction process was monitored by recording changes in the UV-visible absorption spectrum at regular time intervals. At each selected time point, a small volume of the reaction mixture was taken out and diluted with distilled water, and analysed to determine the extent of MO reduction. After the completion of the reaction, the catalyst was efficiently recovered by centrifugation for further reuse.

2.7. General procedure for the degradation of RhB using Ag@CS–BCN nanohybrid as a nanocatalyst

The Ag@CS–BCN (0.06 mol%) nanohybrid was introduced into an aqueous solution of RhB (0.2 mM, 25 mL) under light stirring. Afterwards, a freshly prepared aqueous solution of $NaBH_4$ (0.5 M, 10 mL) was added to the reaction mixture. The degradation process was monitored using a UV-visible spectrophotometer at regular time intervals. At each designated time point, a small volume of the reaction mixture was taken out and diluted with distilled water, and analysed to determine the extent of RhB degradation. After the completion of the reaction, the Ag@CS–BCN nanohybrid was efficiently recovered by centrifugation for further reuse.

2.8. Antimicrobial studies

CS–BCN (AB-Comp) and Ag@CS–BCN nanohybrid (AB-ADS) were tested for antibacterial and antifungal studies. The bacterial strains, such as *Escherichia coli* (*E. coli*) and *Staphylococcus aureus* (*S. aureus*) and the pathogenic yeasts, such as *Cryptococcus neoformans* (*C. neoformans*) and *Candida albicans* (*C. albicans*).

2.9. Procedure of antimicrobial assay

Concerning antibacterial studies, nutrient agar plates (20 mL per plate) were prepared and uniformly infused with a 24 h culture of bacteria and standardised to a 0.5 optical density (OD) value according to the McFarland standard. Wells were sterilised and pierced, and varying concentrations (500, 250, 100, and 50 μg mL^{-1}) of the test compounds CS–BCN and Ag@CS–BCN nanohybrid were introduced into the wells. Gentamicin served as the positive control. The plates were incubated at 37 °C for 24 h. Following incubation, antibacterial efficacy was evaluated by measuring the diameter of the inhibition zones surrounding each well.

For assessing antifungal activity, potato dextrose agar medium (20 mL per plate) was seeded with a 72 h culture of fungal strains in Petri plates, and various concentrations of the samples CS–BCN and Ag@CS–BCN nanohybrid (AB-ADS) (500, 250, 100 and 50 μg mL^{-1}) were added. Amphotericin B was exploited as a positive control. Then, the Petri plates were incubated for 72 h at 28 °C. Afterwards, the incubation of the antifungal activity was measured by the width of the inhibition zone formed around the wells. All measurements were analysed using GraphPad prism software.

2.10. Procedure for minimum inhibitory concentration (MIC) assay

The antibacterial efficacy of the prepared Ag@CS–BCN nanohybrid was scrutinised against *E. coli* and *S. aureus* using the standard broth microdilution technique. All the assays were carried out in sterile 96-well flat-bottomed microtiter plates. A 0.5 McFarland standard suspension was sequentially diluted 1 : 100 with nutrient broth to obtain a final inoculum density of ~5×10^5 CFU mL^{-1}. Serial dilution of Ag@CS–BCN nanohybrid, ranging from 500, 250, 125, 62.5, 31.25, 15.6, 7.8, 3.9, 1.9 and 0.9 μg mL^{-1}, was prepared in nutrient broth. Each microplate well received 50 μL of bacterial suspension of the respective test concentration. Negative control wells contained only nutrient broth and bacterial inoculum, while positive controls contained a standard antibiotic. The plates were incubated at 37 °C for 18 to 24 h, and the growth of the bacteria was quantified spectrophotometrically at 600 nm using a microplate reader. All the measurements were taken in triplicate, and the mean optical density (OD) values were used to calculate the percentage inhibition of bacterial growth.

2.11. Anticancer activity

The Ag@CS–BCN nanohybrid was investigated for *in vitro* cytotoxicity using HeLa and 3T3 cell lines by MTT assay. Cells were cultured in DMEM supplemented with 10% FBS, 100 μg mL^{-1} penicillin, and 100 μg mL^{-1} streptomycin, and maintained at 37 °C in a humidified environment with 5% CO_2. Briefly, both the cells were collected by trypsinisation and pooled in a 15 mL tube. Then the cells were plated at a density of 1×10^5 cells mL^{-1} (200 μL) into the 96-well tissue culture plate in DMEM medium containing 10% FBS and 1% antibiotic solution for 24 to 48 h at 37 °C. The cells were washed with sterile PBS and treated with various concentrations of test samples in a serum-free DMEM medium. Each sample was replicated three times, and the cells were incubated at 37 °C in a humidified 5% CO_2 incubator for 24 h. After incubation, MTT (10 μL of 5 mg mL^{-1}) was added to each well, and the cells were incubated for another 2–4 h until purple precipitates were visible under an inverted microscope. Finally, the medium and MTT (220 μL) were aspirated off the wells and washed with 1× PBS (200 μL). Furthermore, DMSO (100 μL) was added to dissolve formazan crystals, and the plate was shaken for 5 min. The absorbance for each well was measured at 570 nm using a microplate reader, and the percentage cell viability and IC_{50} value were calculated using GraphPad Prism software.

3. Results and discussion

3.1. Synthesis of Ag@CS–BCN nanohybrid

The synthesis of the Ag@CS–BCN nanohybrid involves a multistage process (Scheme 1). Initially, BCN was prepared by mixing melamine and boric acid by mechanical grinding using a mortar and pestle. Followed by calcination at 550 °C for 4 h in a muffle furnace (Scheme 1, A). Chitosan is dissolved in diluted acetic acid to create a chitosan solution (Scheme 1, B). Subsequently, BCN was introduced into this chitosan solution. Then the chitosan was crosslinked with glutaraldehyde, which reacts with the amino groups of the chitosan molecule through Schiff base formation (–C═N–).[34,35] The formation of a 3D network involves the reaction between the aldehyde group (–CHO) and the primary amine group ($-NH_2$) on the chitosan backbone to form imine bonds (C═N).[36–38] Hence, a stable polymeric network is formed.[34] Finally, BCN was incorporated into the chitosan matrix through hydrogen bonding or electrostatic interactions, yielding a reinforced composite designated as CS–BCN (Scheme 1, C).[39] Later, NaOH was dissolved in water and methanol in the ratio of 1 : 1, and $AgNO_3$ was introduced into it to obtain a $AgNO_3$@CS–BCN (Scheme 1, D). Afterwards, ascorbic acid was infused as a mild reducing agent to reduce Ag^{1+} to Ag^0, and the acquired nanohybrid was labelled as Ag@CS–BCN nanohybrid (Scheme 1, E).

3.2. Spectroscopic and microscopic analysis of Ag@CS–BCN nanohybrid

3.2.1. FT-IR and p-XRD analyses. To pinpoint the characteristic functional groups in the prepared crosslinked CS, BCN, CS–BCN matrix, and the final Ag@CS–BCN nanohybrid, we have carried out FT-IR analysis (Fig. 1a). A broad absorption peak observed at ~3284 cm^{-1} is responsible for the amide A band, which arises from the N–H stretching vibrations of hydrogen-

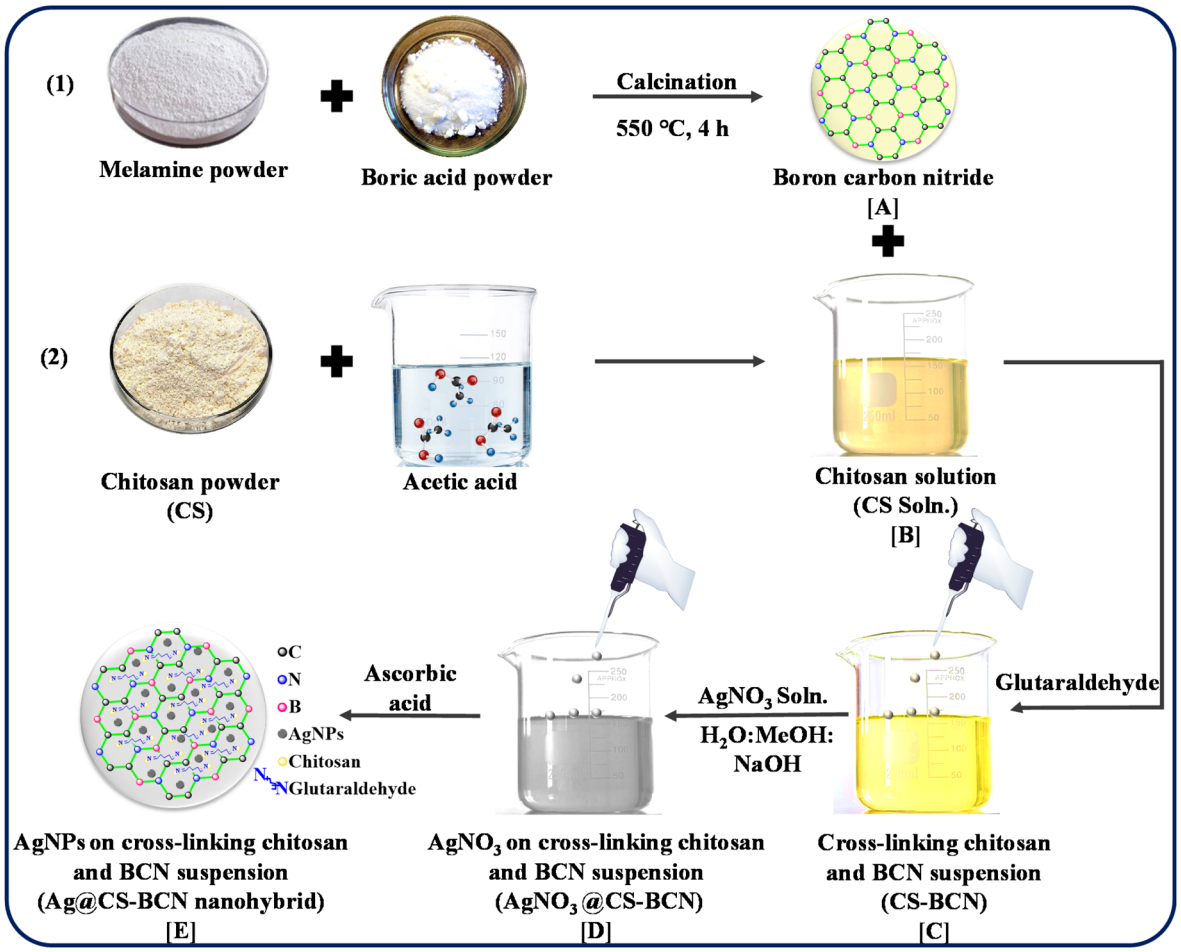

Scheme 1 Synthesis of Ag nanoparticles immobilised on a chitosan matrix crosslinked with glutaraldehyde and functionalized with BCN, forming the Ag@CS–BCN nanohybrid.

bonded amide groups. This peak typically appears in the 3300–3270 cm^{-1} range and indicates the presence of peptide or amide functionalities.[40,41] A strong and broad absorption band near ~3564 cm^{-1} corresponds to O–H stretching vibrations, suggesting the presence of free or hydrogen-bonded hydroxyl groups.[42] A weak to medium intensity band observed at ~2878 cm^{-1} is assigned to the stretching vibrations of aliphatic $-CH_3$ and $-CH_2$ groups.[43,44] Meanwhile, the band at ~2172 cm^{-1} can be assigned to the stretching vibrations of C≡N (nitrile) or C=N groups, often present in heterocycles or Schiff bases.[44] A band at ~1666 cm^{-1} is assigned for the amide I band, primarily due to the C=O stretching vibration of the peptide backbone or amide groups.[40–42] The ~1368 cm^{-1} band reveals the bending vibrations of aliphatic C–H bonds, particularly $-CH_3$ symmetric deformation.[43,44] Finally, a strong peak at ~1054 cm^{-1} is attributed to C–O stretching, often arising from alcohols, esters, or ether functionalities, confirming the presence of oxygenated groups.[43]

The crystalline nature and phase composition of the synthesised samples were investigated using *p*-XRD, as shown in Fig. 1b. In Fig. 1b(i), the two broad diffraction humps found around 25.92° and 43.5° are assigned to the (002) and (100) planes of graphitic-like carbon structures, respectively. The broad nature of these peaks indicates the amorphous or poorly ordered nature of the carbon framework, typical of boron-doped carbon nitride (BCN) and similar disordered graphitic materials.[45–47] The (002) reflection at ~25.9° corresponds to the interlayer stacking of carbon nitride sheets, while the (100) peak at ~43.5° is attributed to in-plane ordering of the carbon network. The absence of sharp peaks suggests that BCN exists in a partially crystalline or turbostratic phase, with disrupted π–π stacking due to boron doping and heteroatom incorporation, which reduces the regularity of the graphitic layers.[46] Fig. 1b(ii) shows the diffraction pattern of chitosan. The p-XRD pattern of chitosan exhibits two prominent reflections at 2θ ~ 9.2° and ~20.6°, indicating its semi-crystalline nature. The peak at 9.2° corresponds to the (020) plane, which is associated with the hydrated crystalline domains of chitosan, resulting from intermolecular hydrogen bonding between polymer chains.[48,49] The more intense and sharper peak at 20.6° is attributed to the (120) crystallographic plane of chitosan, reflecting its intrinsic crystallinity and chain packing regularity in the dry state.[49,50] The prominent reflections at 2θ values corresponding to planes indexed to a face-centred cubic (FCC) structure of metallic Ag,

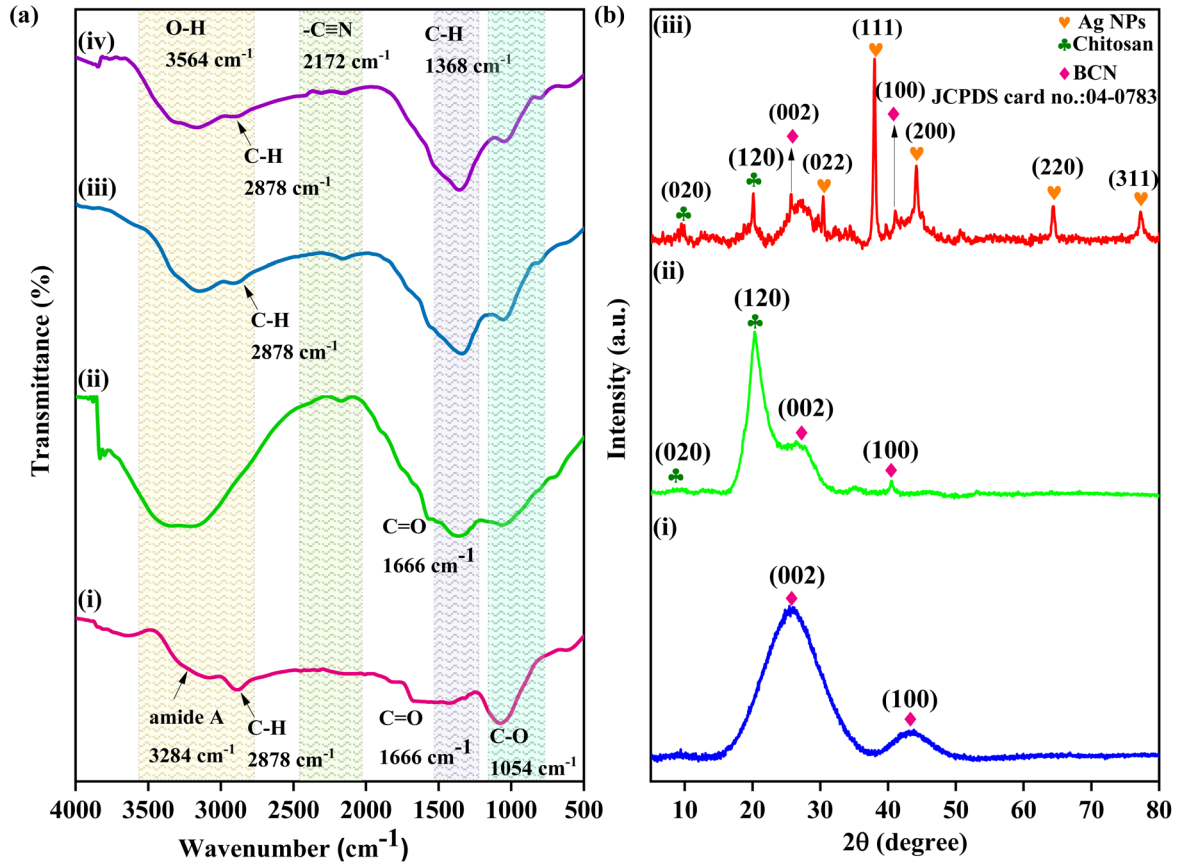

Fig. 1 (a) FT-IR spectra of (i) CS, (ii) BCN, (iii) CS–BCN, and (iv) Ag@CS–BCN nanohybrid; (b) *p*-XRD pattern of (i) BCN, (ii) CS–BCN, and (iii) Ag@CS–BCN nanohybrid.

matching well with the JCPDS card number 04-0783. The major peaks appear at approximately 38.11°, 44.27°, 64.42°, and 77.42°, corresponding to the crystalline planes of (111), (200), (220), and (311) planes of FCC AgNPs.[51,52] In addition to the typical Ag peaks, a noticeable reflection at $2\theta = 30.38°$ is observed, which corresponds to the (022) crystal plane. This peak may indicate the formation of a secondary phase, possibly due to partial oxidation, metal oxide formation, or interaction with a support matrix such as silicates or heteroatom-doped carbon. Such features are often seen in Ag-based hybrid nanostructures, where the presence of (022) planes has been reported in doped or supported Ag systems, suggesting structural modification or lattice distortion within the composite.[53]

3.2.2. FE-SEM and HR-TEM analyses. The morphological and structural features of the prepared BCN, CS–BCN, and Ag@CS–BCN nanohybrids were examined using FE-SEM, TEM, HR-TEM, SAED, and EDX elemental mapping, as shown in Fig. 2. The FE-SEM image of BCN (Fig. 2a) displays a layered morphological characteristic of 2D boron carbonitride nanosheets.[54] In Fig. 2b, the CS–BCN nanohybrid shows that CS was covered with BCN sheets with a roughened, thicker morphology due to chitosan incorporation, suggesting successful interfacial interactions between the amine groups of chitosan and the electronegative sites of BCN through hydrogen bonding or electrostatic attraction.[48,55] The Ag@CS–BCN nanohybrid (Fig. 2c) exhibits a granular and agglomerated surface, with spherical Ag nanoparticles uniformly distributed over the CS–BCN matrix, confirming efficient nucleation and stabilisation of silver nanoparticles on the CS–BCN support.[56] The TEM image of CS–BCN (Fig. 2d) shows thin folded nanosheets, confirming the presence of thin BCN layers intercalated or functionalized by polymeric chitosan. The Ag@CS–BCN sample (Fig. 2e) displays AgNPs (dark spots) well-dispersed over the CS–BCN matrix, indicating effective anchoring and distribution of AgNPs within the CS–BCN matrix. The HR-TEM image (Fig. 2f) reveals lattice fringes with an interplanar spacing of 0.26 nm, corresponding to the (111) plane of face-centred cubic (FCC) Ag, confirming the crystalline nature of AgNPs.[48,54] The SAED pattern (Fig. 2g) of Ag@CS–BCN shows distinct diffraction rings/spots, verifying the polycrystalline nature of AgNPs embedded within the CS–BCN matrix. Further, the HAADF-STEM image combined with elemental mapping (Fig. 2h) confirms the homogeneous distribution of B, C, N, O, and Ag elements in the nanohybrid. The distinct and overlapping elemental maps demonstrate the successful interaction between AgNPs and the CS–BCN matrix. The presence of nitrogen and oxygen further supports the effective incorporation of chitosan, while the intense signal from Ag corroborates the successful reduction and immobilisation of Ag on the CS–BCN matrix.[57,58]

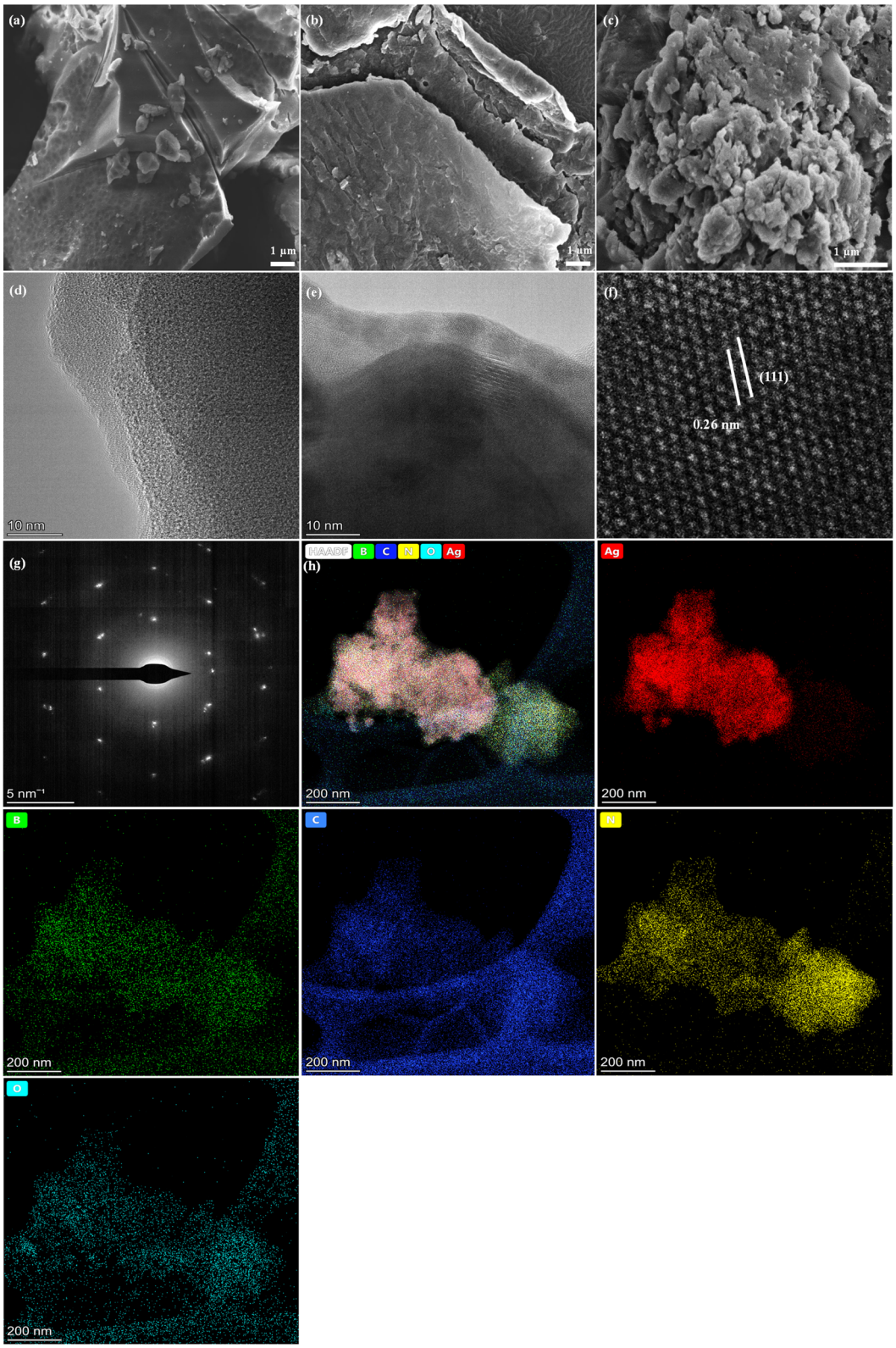

Fig. 2 FE-SEM images of (a) BCN, (b) CS–BCN, and (c) Ag@CS–BCN nanohybrid; TEM images of (d) CS–BCN, (e) Ag@CS–BCN nanohybrid, (f) HR-STEM image of Ag@CS–BCN nanohybrid, (g) SAED pattern of Ag@CS–BCN nanohybrid and (h) HAADF image of Ag@CS–BCN nanohybrid.

3.2.3. XPS analysis. The X-ray photoelectron spectroscopy (XPS) analysis of Ag@CS–BCN nanohybrid was provided in (Fig. 3) and gives the detailed insights into its elemental composition and surface chemical states. The survey spectrum revealed the distinct peaks corresponding to C, O, N, B, and Ag, confirming the successful incorporation of AgNPs onto the CS–BCN matrix with

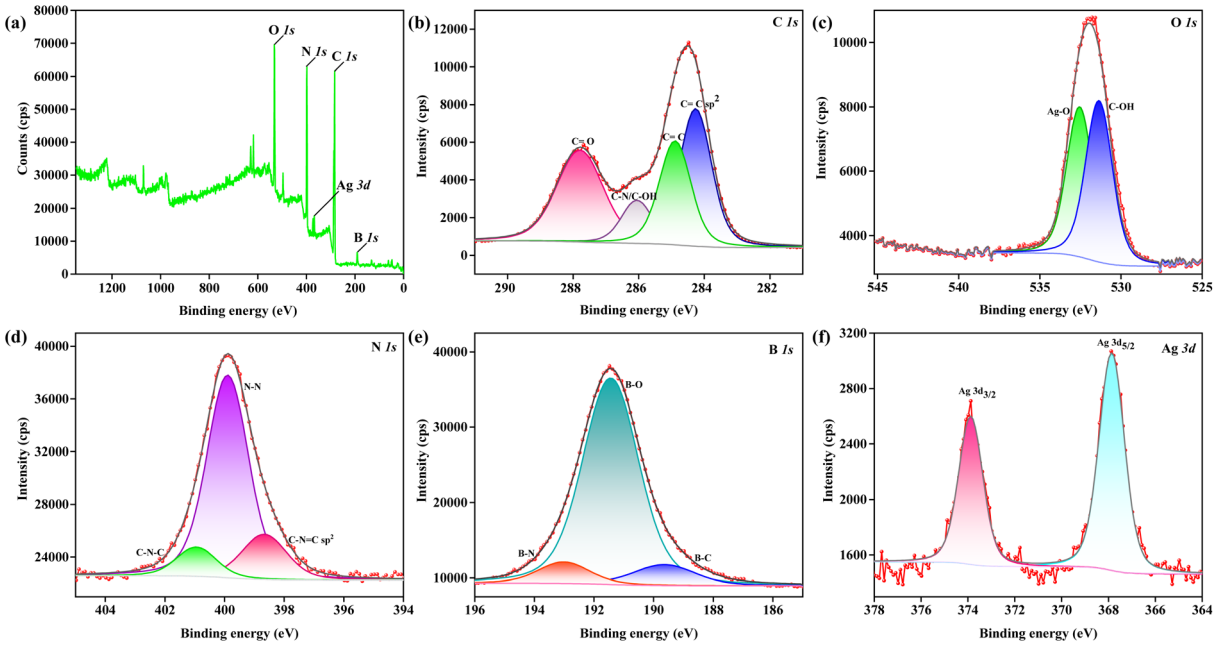

Fig. 3 (a) XPS survey spectrum of Ag@CS–BCN nanohybrid and comparative high resolution XPS spectra of (b) C 1s, (c) O 1s, (d) N 1s, (e) B 1s, and (f) Ag 3d.

high purity. The deconvoluted C 1s spectrum displayed the peaks at 284.2 eV, 284.8 eV, 286.0 eV, and 287.7 eV corresponding to C=C sp^2 hybridised carbon, C–C, C–N/C–OH, and C=O bonds, respectively, indicating the existence of partially oxidised carbon functionalities that promote metal anchoring.[59,60] The O 1s spectrum exhibited peaks around 531.3 eV and 532.5 eV, attributed to metal–oxygen (Ag–O) interactions and surface oxygen-containing groups, suggesting a strong interfacial bonding between AgNPs and the CS–BCN matrix.[61,62] The N 1s deconvoluted peaks revealed at 398.6 eV, 399.8 eV, and 400.9 eV belong to sp^2 hybridised nitrogen (C=N–C (graphitic-N)), pyrrolic-N (N–N), and quaternary-N (C–N–C).[63,64] In comparison, the B 1s high-resolution spectrum showed peaks around 189.6 eV, 191.4 eV, and 193.0 eV attributed to B–C bonds within the BCN lattice, indicating strong boron–carbon interactions, B–O bonds arising from surface oxidation or residual boron oxide species, and B–N bonds confirming the formation of boron-nitrogen linkages within the BCN, which confirms the structural integrity.[65] The Ag 3d high-resolution XPS spectrum displayed two well-defined peaks at 367.8 eV (Ag $3d_{5/2}$) and 373.8 eV (Ag $3d_{3/2}$), characteristics of metallic Ag^0, and slight shifts suggested a minor contribution from surface oxidised Ag^+ species.[66,67] The XPS high-resolution spectra collectively confirm that AgNPs are uniformly anchored on the CS–BCN matrix through oxygen- and nitrogen-containing linkages.

3.2.4. ICP-OES analysis. ICP-OES was employed to determine the silver content in the Ag@CS–BCN nanohybrid, revealing a silver loading of 1.42% w/w.

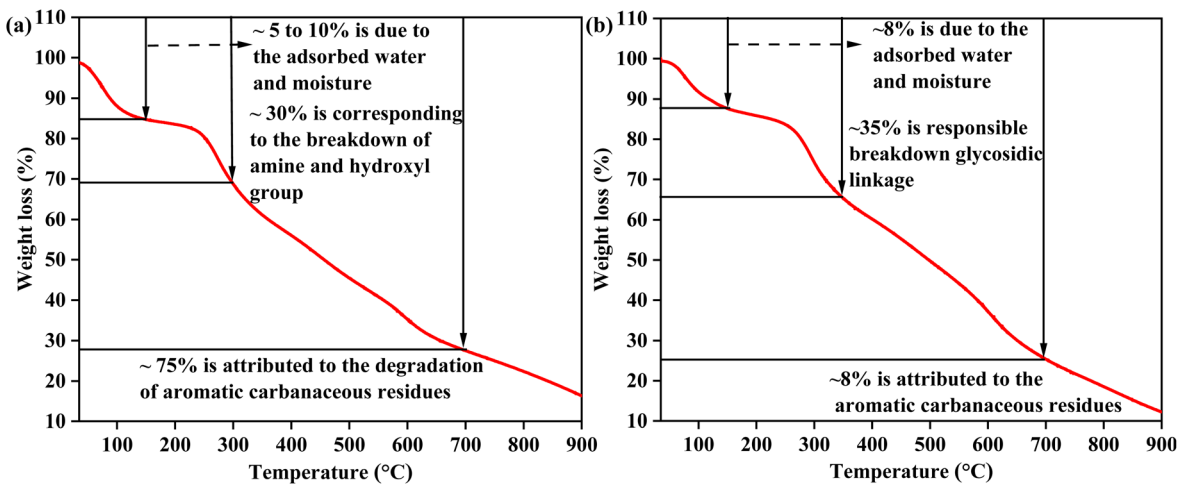

Fig. 4 TG curves of (a) CS–BCN and (b) Ag@CS–BCN nanohybrid.

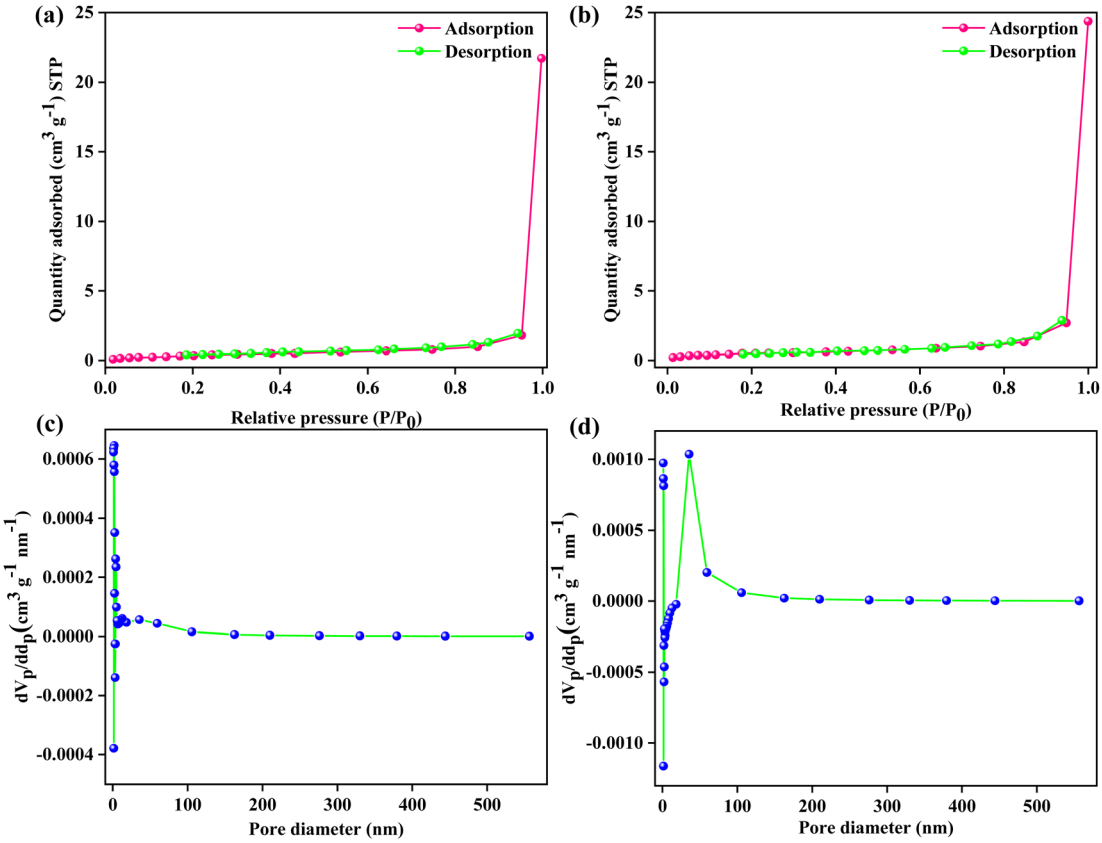

Fig. 5 Nitrogen adsorption–desorption isotherm curves for (a) CS–BCN and (b) Ag@CS–BCN nanohybrid; BJH pore size distribution plot of (c) CS–BCN and (d) Ag@CS–BCN nanohybrid.

3.2.5. Thermogravimetric (TG) analysis. The thermal stability of the CS–BCN matrix and Ag@CS–BCN nanohybrids was investigated by TG analysis shown in Fig. 4. The TG curve of CS–BCN (Fig. 4a) exhibits a three-step degradation pattern. The first weight loss below ~150 °C is attributed to the removal of physically adsorbed water and moisture (hydroxyl groups).[68] The second major weight loss between 200–400 °C is due to the decomposition of the chitosan backbone, including depolymerisation and degradation of its acetylated and deacetylated units.[48] The third stage, occurring beyond 500 °C, corresponds to the breakdown of residual organic matter and partial degradation or oxidation of the BCN framework.[69] In the case of Ag@CS–BCN nanohybrid (Fig. 4b), a shift in degradation to higher temperatures is observed, indicating enhanced thermal stability. This improved resistance is likely due to the strong interaction between AgNPs and the functional groups in chitosan, which may hinder polymer chain motion and suppress thermal degradation.[69,70] Furthermore, the presence of AgNPs promotes structural rigidity within the nanohybrid.

3.2.6. BET surface area analysis. The nitrogen adsorption–desorption isotherms of both CS–BCN (Fig. 5a) and Ag@CS–BCN (Fig. 5b) exhibit type IV isotherms with H3 hysteresis loops, indicative of mesoporous structures. The H3 loop is commonly associated with slit-like pores formed by the aggregation of plate-like particles, which is consistent with the layered BCN structure and chitosan crosslinking matrix.[71] The CS–BCN matrix and Ag@CS–BCN nanohybrid have a specific surface area of 2.1 $m^2 g^{-1}$ and 1.7 $m^2 g^{-1}$. The BJH pore size distribution curves of CS–BCN matrix and Ag@CS–BCN nanohybrid were shown in Fig. 5c and d, respectively, and possess an average pore diameter of 10.4 nm and 54.2 nm.

3.3. Catalytic investigation of Ag@CS–BCN nanohybrid as a nanocatalyst in the reduction of nitroarenes

The Ag@CS–BCN nanohybrid was initially employed for the reduction of mono- and di-nitroarenes, with the extensively studied 4-NP to 4-AP transformation adopted as the model reaction.

3.3.1. Reduction of 4-NP to 4-AP. To evaluate the catalytic performance of the synthesised Ag@CS–BCN nanohybrid, its activity was assessed in the reduction of 4-NP to 4-AP in an

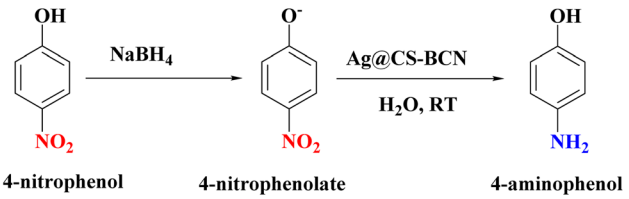

Scheme 2 The catalytic activity of Ag@CS–BCN nanohybrid in the reduction of 4-NP to 4-AP using $NaBH_4$ under ambient conditions.

Table 1 Optimisation of the reaction parameters for the $NaBH_4$-mediated reduction of 4-NP was conducted in the presence of Ag@CS–BCN nanohybrid[a]

Entry	4-NP (mM)	$NaBH_4$ (M)	Ag@CS–BCN (mol% of Ag)	Time (min)
1	2.5	—	0.08	60[b]
2	2.5	0.4	—	60[c]
3	2.5	0.3	0.08	10
4	2.5	0.4	0.13	17
5	2.5	0.4	0.10	6
6	**2.5**	**0.4**	**0.08**	**5**
7	2.5	0.4	0.07	5
8	2.5	0.4	0.06	5
9	2.5	0.45	0.08	4
10	2.5	0.5	0.08	5
11	2.5	0.45	15 mg[d]	15[b]

[a] Reaction conditions: 4-NP (10 mL), $NaBH_4$ (10 mL), Ag@CS–BCN nanohybrid as a nanocatalyst in water at room temperature. [b] No reaction. [c] Incomplete reaction. [d] CS–BCN as a catalyst.

aqueous medium, using $NaBH_4$ as the reducing agent at room temperature, as demonstrated in Scheme 2. The reaction progress was monitored at regular time intervals using UV-visible spectroscopy, taking advantage of the distinct absorption maxima of the 4-NP, 4-nitrophenolate, and 4-AP. Initially, the yellow solution of 4-NP exhibits a characteristic absorption peak at 316 nm. Upon the introduction of freshly prepared aqueous $NaBH_4$, the yellow colouration intensifies due to the formation of 4-nitrophenolate, accompanied by a red shift in absorbance, maintaining the peak at 400 nm. As the reduction proceeds in the presence of Ag@CS–BCN nanohybrid, a gradual decline in the 4-nitrophenolate peak was observed, along with the appearance of the new peak at 295 nm, corresponding to 4-AP. The optimisation of the reaction conditions, including variations in $NaBH_4$ concentrations and catalyst loading, was systematically carried out and is presented in Table 1. No reduction was observed in the absence of $NaBH_4$ (Table 1, entry 1; Fig. 6a). The Ag@CS–BCN nanohybrid alone facilitated a shift in equilibrium toward the formation of 4-nitrophenolate but didn't drive the complete reaction. Conversely, in the absence of Ag@CS–BCN nanohybrid, the reaction remained largely incomplete, achieving only 65.98% conversion even after 1 h (Table 1, entry 2; Fig. 6b). Notably, the combined presence of both Ag@CS–BCN nanohybrid and $NaBH_4$ markedly enhanced the reduction efficiency (Table 1, entries 4–8). This indicates

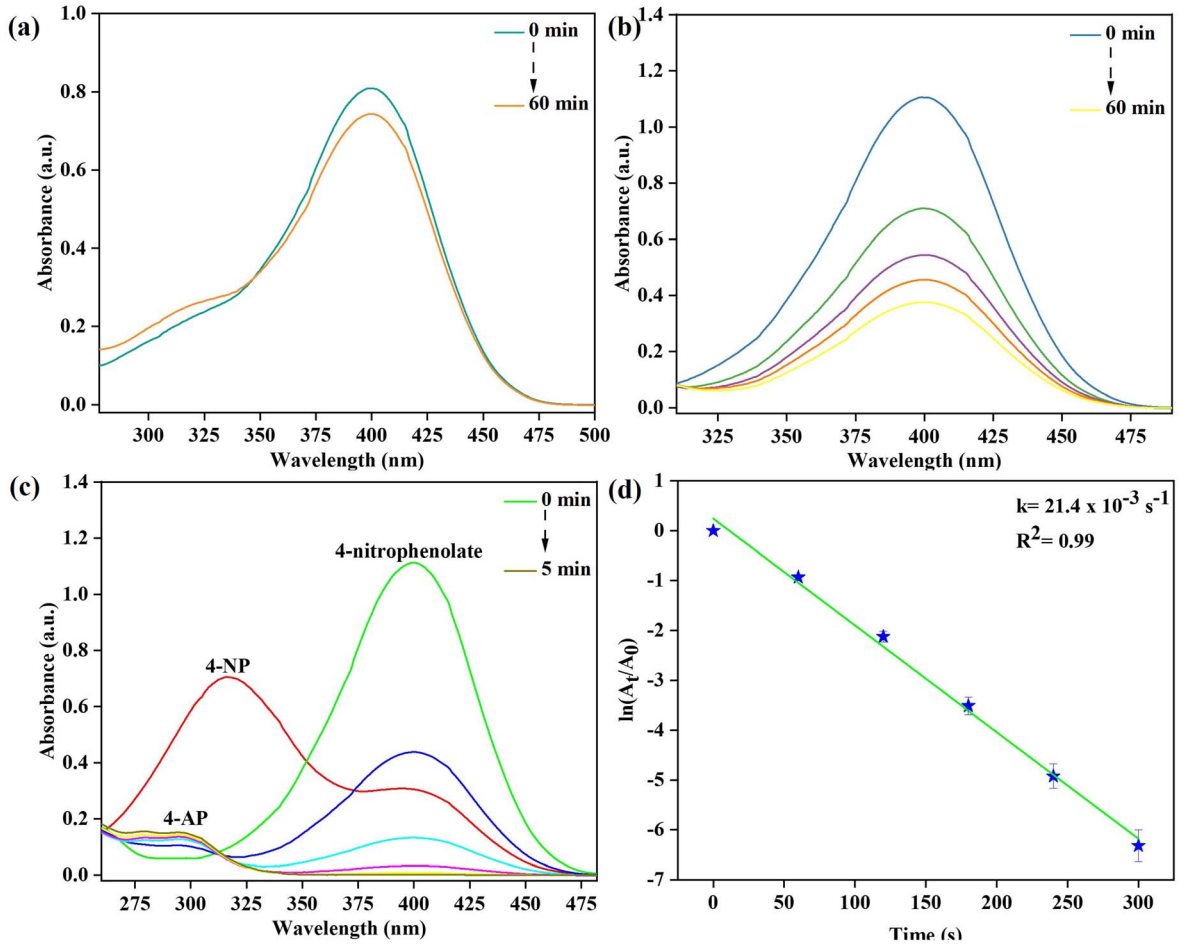

Fig. 6 UV-visible spectra illustrating the reduction of 4-NP under various conditions (a) in the absence of $NaBH_4$, (b) without Ag@CS–BCN nanohybrid, (c) in the presence of both $NaBH_4$ and Ag@CS–BCN nanohybrid under optimised conditions and (d) the corresponding kinetic plot of $\ln(A_t/A_0)$ *versus* time.

that both $NaBH_4$ and Ag@CS–BCN nanohybrid are essential for effective reduction. Optimal catalytic activity was observed with 0.08 mol% Ag of Ag@CS–BCN nanohybrid and 0.4 M $NaBH_4$, where complete conversion 99.82% of 4-NP to 4-AP was achieved within just 5 min (Table 1, entry 5; Fig. 6c). To confirm the catalytic role of AgNPs, a control experiment was conducted using CS–BCN (Table 1, entry 9) which showed no significant reduction even after 1 h. The reduction reaction followed *pseudo-first-order* kinetics, facilitated by excess $NaBH_4$. The apparent rate constant was determined to be 21.4×10^{-3} s^{-1} with a correlation coefficient (R^2) of 0.99 (Fig. 6d).

3.3.2. Reduction of various nitroarenes. Following the reduction of 4-NP under aqueous $NaBH_4$ and ambient temperature, the established optimal conditions were extended to study the catalytic proficiency of the Ag@CS–BCN nanohybrid as a nanocatalyst towards a series of structurally diverse mono- and di-nitroarenes. An aqueous medium was deliberately chosen, aligning with the green chemistry principles and offering the dual advantage of serving as an eco-friendly reaction medium while simultaneously addressing environmental concerns through potential wastewater remediation applications. The reduction of nitroarenes (2.5 mM, 10 mL) was carried out in the presence of $NaBH_4$ (0.4 M, 10 mL) using Ag@CS–BCN nanohybrid (0.08 mol%) at room temperature. The progress of each reduction reaction was monitored by observing the variation in the absorbance at the characteristic λ_{max} of the respective nitroarene derivatives, which is displayed in Fig. S1. The extent of the conversion was quantified by averaging the results from multiple experiments, ensuring statistical reliability and reproducibility. A wide range of functional substituents spanning both electron-donating (–NH_2, –OH, –CH_2OH) and electron-withdrawing (–NO_2, –$COCH_3$, –COOH) groups were

Table 2 Reduction of nitroarenes to corresponding aromatic amines using $NaBH_4$ in the presence of AgNPs@CS–BCN nanohybrid[a]

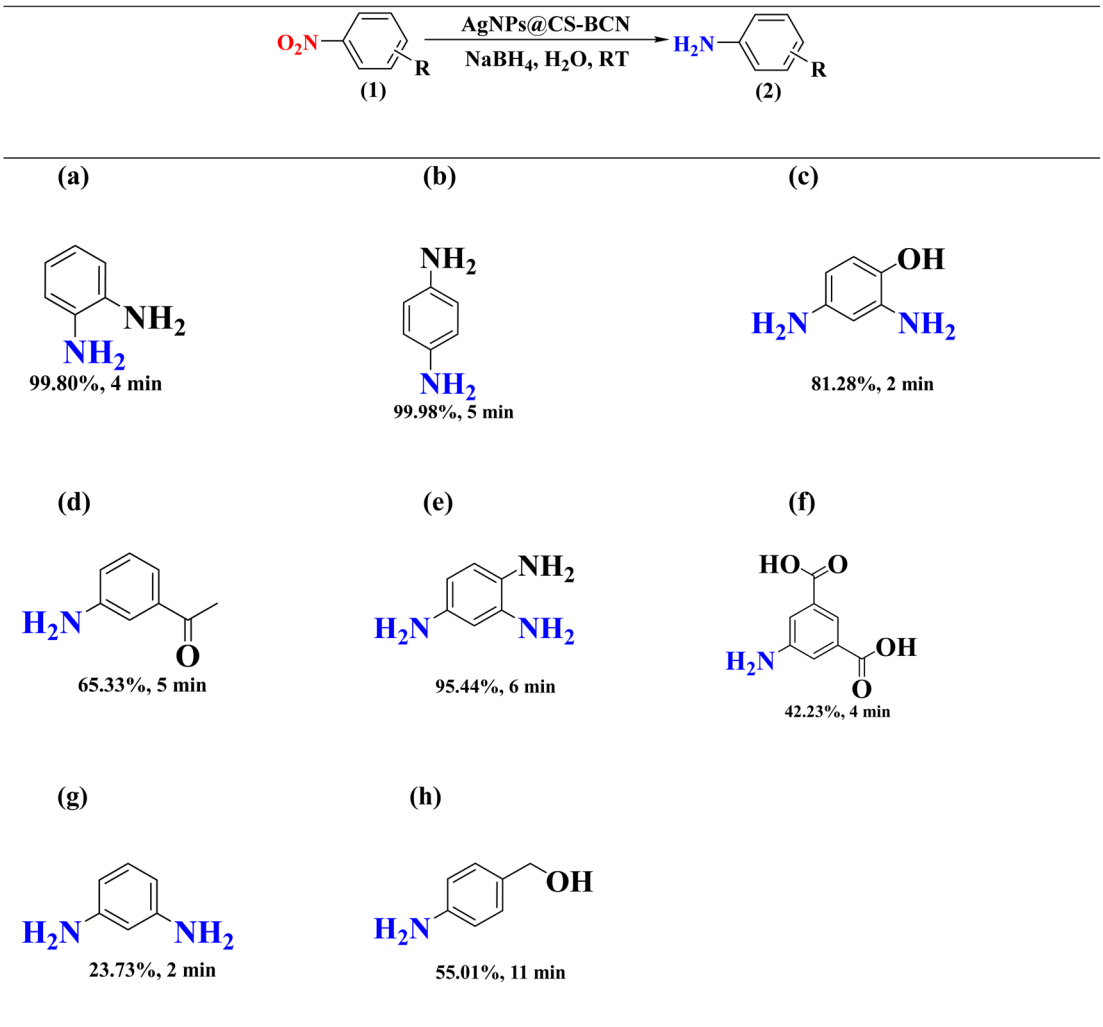

[a] Reaction Condition: nitroarenes (2.5 mM, 10 mL), aqueous $NaBH_4$ (0.4 M, 10 mL), AgNPs@CS–BCN nanohybrid (0.08 mol%) in water and room temperature.

systematically explored to investigate their influence on the reduction kinetics and overall catalytic efficacy. Remarkably, the Ag@CS–BCN nanohybrid exhibited excellent catalytic activity across all substrates, with rapid reductions observed in minimal time. The nanocatalyst maintained high activity regardless of the substituent's electronic nature or steric profile, highlighting its robustness and adaptability. The mono-nitroarenes, including 2-nitroaniline, 4-nitroaniline, 4-nitrobenzyl alcohol, and 3-nitroacetophenone (Table 2a, b, d and h), were efficiently reduced by the Ag@CS–BCN nanohybrid within short time frames. Among them, 2-nitroaniline exhibited a faster reduction rate compared to its *para*-substituted isomer, 4-nitroaniline, despite the expected steric hindrance at the *ortho* position. This behaviour can be attributed to the intramolecular hydrogen bonding between the *ortho*-positioned $-NH_2$ and $-NO_2$ groups in 2-nitroaniline, which facilitates greater planarity and conjugation across the aromatic ring. 4-Nitrobenzyl alcohol was rapidly converted, and possibly assisted by the weak electron-donating effect of the $-CH_2OH$ group. On the other hand, 3-nitroacetophenone took slightly longer to reduce, consistent with the presence of an electron-withdrawing $-COCH_3$ group that deactivates the aromatic ring toward nucleophilic attack. The di-nitroarenes (Table 2c, e and g) exhibited slower conversion kinetics due to the presence of two electron-withdrawing groups, which reduce the electron density of the aromatic system. However, the catalyst still demonstrated excellent activity. 2,4-Dinitroaniline was reduced efficiently, aided by the electron-donating $-NH_2$ group, which enhances electron delocalisation and facilitates hydride transfer. 2,4-Dinitrophenol required a longer reaction time, possibly due to intramolecular hydrogen bonding and resonance stabilisation from the –OH group. 1,3-Dinitrobenzene was partially reduced. While the 5-nitroisophthalic acid (Table 2f) took the longest, attributed to the presence of –COOH groups, which strongly withdraw electron density and hinder the reduction process. Overall, mono-nitroarenes showed faster and more efficient reduction profiles compared to di-nitro derivatives. These findings affirm the high versatility and catalytic efficiency of Ag@CS–BCN across a wide spectrum of nitroarene substrates.

3.3.3. Degradation of MO and RhB. The widespread discharge of synthetic organic dyes into the environment has become a major contributor to water pollution, underscoring the urgent need for effective removal strategies. In pursuit of sustainable environmental remediation, we explored the

Table 3 Optimisation of reaction parameters for the reduction and degradation of MO using $NaBH_4$ in the presence of Ag@CS–BCN nanohybrid[a]

Entry	MO (mM)	$NaBH_4$ (M)	Ag@CS–BCN (mol% of Ag)	Time (min)
1	0.2	—	0.08	60[b]
2	0.2	0.4	—	60[c]
3	0.2	0.2	0.08	18
4	0.2	0.3	0.08	10
5	0.2	0.4	0.08	7
6	**0.2**	**0.45**	**0.08**	**3**
7	0.2	0.2	0.26	30
8	0.2	0.2	0.13	20
9	0.2	0.2	0.07	16

[a] Reaction conditions: MO (25 mL), $NaBH_4$ (10 mL), Ag@CS–BCN nanohybrid as a nanocatalyst in water at room temperature. [b] No reaction. [c] Incomplete reaction.

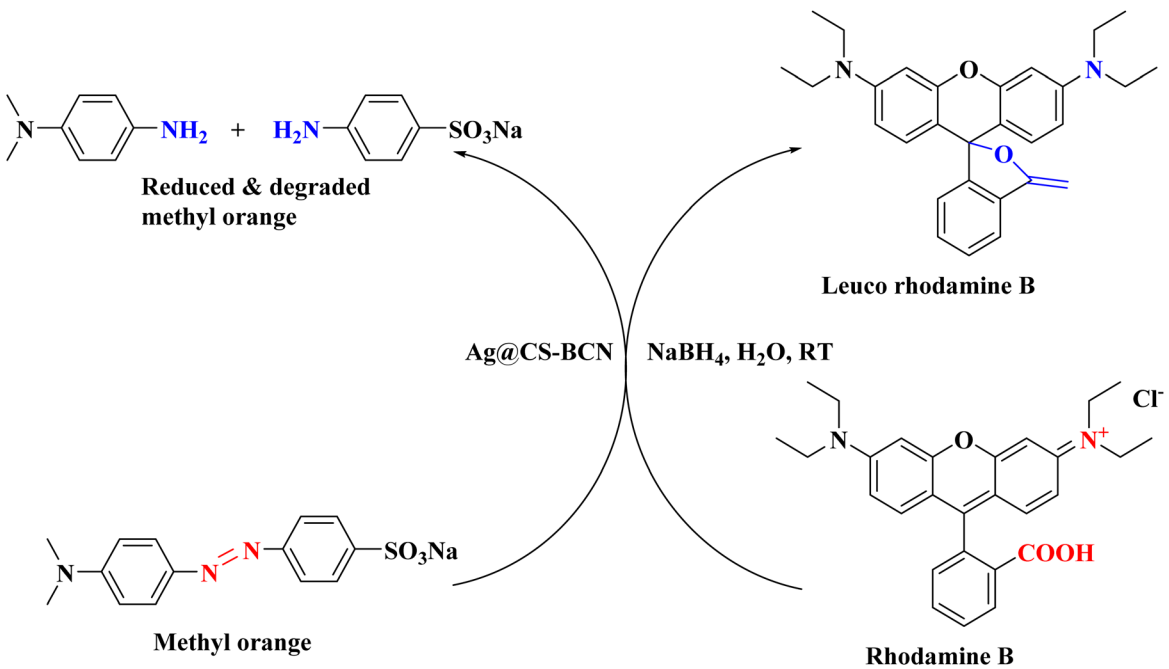

Scheme 3 Reduction and degradation of MO & RhB dye into its reduced and degraded forms using $NaBH_4$ solution and in the presence of Ag@CS–BCN nanohybrid at room temperature.

Table 4 Optimisation of experimental variables for the reduction and degradation of RhB using $NaBH_4$ in the existence of Ag@CS–BCN nanohybrid[a]

Entry	RhB (mM)	$NaBH_4$ (M)	Ag@CS–BCN (mol% of Ag)	Time (min)
1	0.2	—	0.06	60[b]
2	0.2	0.5	—	20
3	0.2	0.2	0.26	38
4	0.2	0.3	0.06	28
5	0.2	0.4	0.06	12
6	**0.2**	**0.5**	**0.06**	7
7	0.2	0.2	0.06	28
8	0.2	0.2	0.13	38
9	0.2	0.2	0.08	30

[a] Reaction conditions: RhB (25 mL), $NaBH_4$ (10 mL), Ag@CS–BCN nanohybrid as a nanocatalyst in water at room temperature. [b] No reaction.

catalytic performance of the Ag@CS–BCN nanohybrid in facilitating the reduction and degradation of MO and RhB, typical prototypical anionic and cationic dye pollutants. The degradation process employing $NaBH_4$ as a reducing agent was catalysed by the least amount of Ag@CS–BCN nanohybrid (Scheme 3). Initially, a defined amount of Ag@CS–BCN nanohybrid was dispersed to accomplish the adsorption equilibrium. Consequently, a freshly prepared aqueous $NaBH_4$ was added, and the reaction progress was monitored using UV-visible spectroscopy within the characteristic absorption maxima zone λ_{max} of 461 nm and 552 nm for MO and RhB. The evolution of the reduction process was indicated by a marked decrease in absorbance, corresponding to the formation of a colourless degradation derivative. The optimisation of the reaction conditions was recognised by varying the concentration of $NaBH_4$ solution and the amount of catalyst loading in Tables 3 and 4. Without $NaBH_4$, the degradation of MO and RhB showed no sign of reduction (Tables 3 and 4, entry 1; Fig. 7a and 8a). In contrast, in the absence of Ag@CS–BCN nanohybrid, the degradation reaction remains incomplete even after 60 min, with the conversion of 48.09% for MO, and reduction took place within 20 min for RhB with the % conversion of 99.07% (Tables 3 and 4, entry 2; Fig. 7b and 8b). The optimal degradation of MO from its orange form to a reduced, colourless product was achieved with a 94.50% conversion in 3 min using 0.45 M $NaBH_4$ and 0.08 mol% of Ag@CS–BCN nanohybrid (Table 3, entry 6; Fig. 7c). For the reduction of RhB from red to leuco RhB

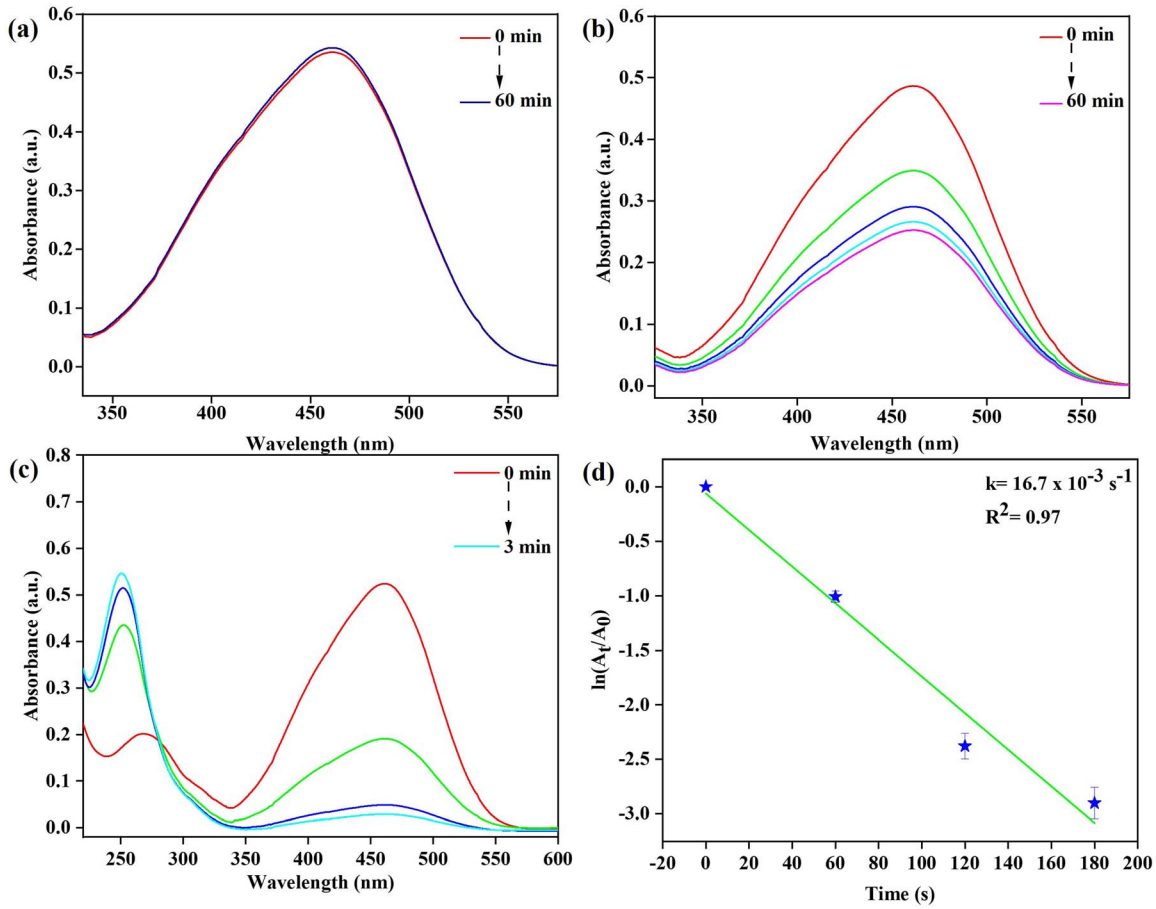

Fig. 7 UV-visible spectra demonstrating the reduction and degradation of MO under various conditions: (a) in the absence of $NaBH_4$, (b) without Ag@CS–BCN nanohybrid, (c) in the presence of both $NaBH_4$ and Ag@CS–BCN nanohybrid, and (d) the corresponding kinetic plot of $\ln(A_t/A_0)$ *versus* time.

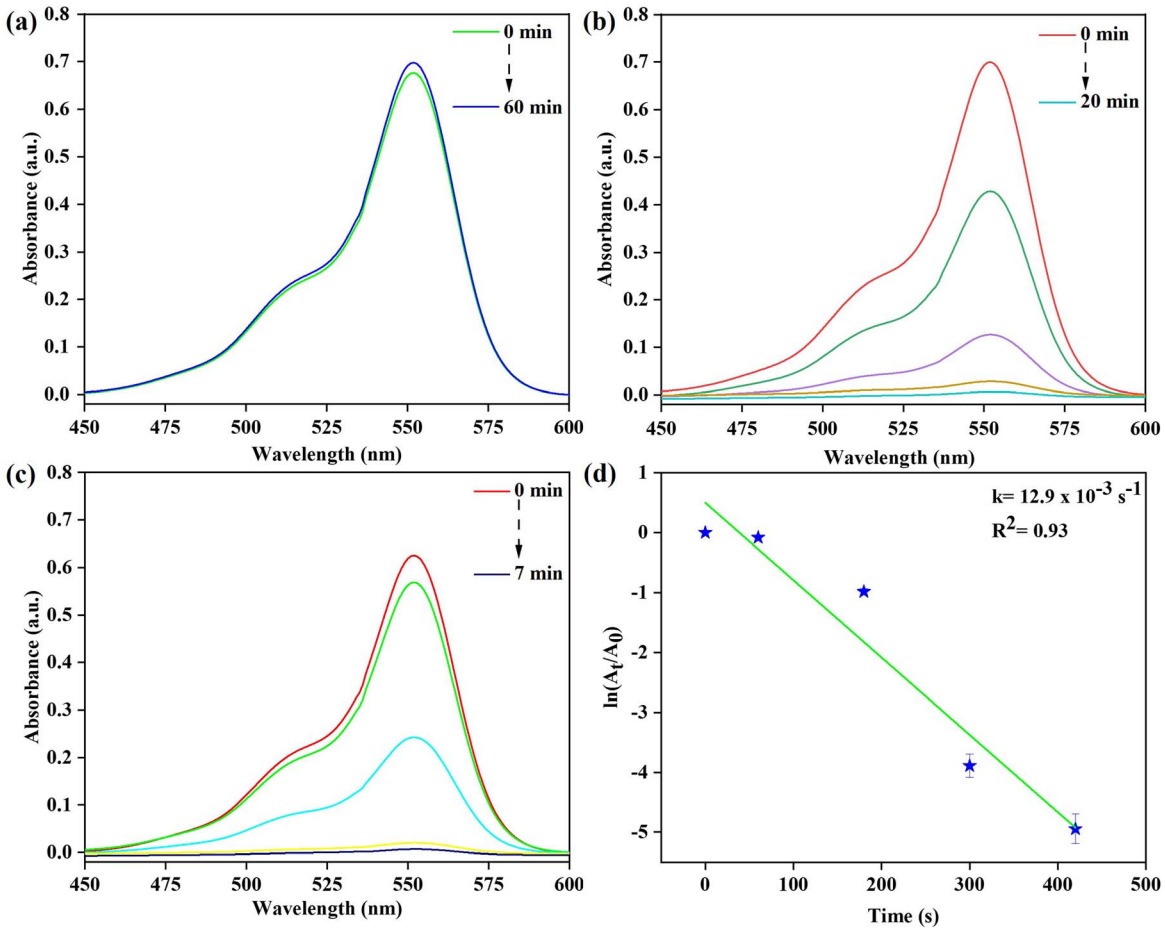

Fig. 8 UV-visible spectra demonstrating the reduction and degradation of RhB to leuco RhB under various conditions in the absence of: (a) $NaBH_4$, (b) Ag@CS–BCN nanohybrid, and (c) in the presence of both $NaBH_4$ and Ag@CS–BCN nanohybrid, and (d) the corresponding kinetic plot of $\ln(A_t/A_0)$ *versus* time.

(colourless), a 98.89% conversion efficiency was reached in 7 min using 0.5 M $NaBH_4$ and 0.06 mol% of Ag@CS–BCN nanohybrid (Table 4, entry 6; Fig. 8c) These results highlighting the necessity of both the components for rapid and efficient dye reduction reactions (Tables 3 and 4, entries 3–9). Analogous to the reduction of 4-NP, the reduction and degradation of MO & RhB followed *pseudo-first-order* kinetics, exhibiting rate constants of 16.7×10^{-3} s^{-1} and 12.9×10^{-3} s^{-1}, respectively and corresponding R^2 values of 0.97 and 0.93 (Fig. 7d and 8d). Nevertheless, in the case of RhB, the reaction mixture gradually regained the pastel pink colour due to aerial oxidation, which can be attributed to the reversible lactonic ring opening of leuco RhB.

3.4. Plausible mechanism for the reduction/degradation using Ag@CS–BCN nanohybrid

Scheme S1 presents the plausible mechanism for the catalytic reduction of 4-nitrophenol (model) using Ag@CS–BCN nanohybrid. In this reaction system, $NaBH_4$ serves as the hydride source (electron donor), while the nitro group acts as an electron acceptor. The reduction proceeds *via* the formation of the hydride ion in alkaline conditions, which facilitates electron transfer.[72–74] The Ag@CS–BCN nanohybrid plays an important role in mediating this transfer by enabling the generation and relay of hydride ions. Specifically, the hydrolysis of $NaBH_4$ in aqueous solution leads to the formation of active metal hydride species around the well-dispersed AgNPs embedded in the CS–BCN matrix.[75] These AgNPs serve as catalytic hotspots, promoting the efficient and continuous transfer of hydride ions to the nitro group, thereby reducing it to an amino group. Once the reduction is complete, the products desorb from the catalyst surface, freeing active sites for further catalytic cycles.[76,77] The high dispersion of AgNPs and the synergistic interaction between the metal and the CS–BCN support contribute to the remarkable recyclability and efficiency of the nanocatalyst.

The illustration of Scheme S2 demonstrates catalytic reduction and degradation of organic dyes such as MO and RhB. In this system, the reduction and degradation of MO and RhB dyes are aided by Ag@CS–BCN nanohybrid operating as an electron relay between the donor ($NaBH_4$) and the acceptor (dye molecule). Upon the addition of aqueous solution, MO and RhB molecules first adsorb onto the surface of the Ag@CS–BCN nanohybrid. Subsequent addition of $NaBH_4$ generates hydride ions (OH^-), which form metal hydride bonds around the AgNPs

Table 5 Comparative analysis of Ag@CS–BCN nanohybrid with other silver-based catalysts in the reduction and degradation of 4-NP, MO, and RhB using aqueous $NaBH_4$

Substrate	Catalyst	Catalyst loading (mg)	Time (min)	k (10^{-2} s^{-1})	k_{nor} (s^{-1} g^{-1})	Ref.
4-NP	Ag/TiO_2 NPs	3	3	4.9	1.6	81
	AgRGO	0.2	3	2.3	1.6	82
	MG-AgNPs	3	15	0.3	0.1	83
	Fe_3O_4@PDA@Ag	10	4	1.7	0.2	84
	Ag@CS–BCN	**18**	**5**	2.14	0.1	**Present work**
MO	Fe_3O_4@PDA@Ag	10	4	0.7	0.1	84
	CR-AgNPs	25	15	18.6	0.7	85
	SS-AgNPs	20 μL	16	0.3	0.01	86
	Fe/Cu/Ag 5 : 1 : 0.2	10	1	45.9	4.59	87
	Ag@CS–BCN	**15**	**3**	1.67	0.1	**Present work**
RhB	AgNPs/NCDs	8	2.5	2.9	0.4	88
	Fe_3O_4/SiO_2-Pr-S-Ag	2	0.6	6.4	3.2	89
	CAg-nPs	2.1	17	1.4	0.7	90
	Ag-NPs	50 μL	32	5.9	0.1	91
	Ag@CS–BCN	**20**	**7**	1.29	0.06	**Present work**

via localised hydrolysis. These hydrides are then transferred to the adsorbed dye molecules, reducing MO into colourless intermediates and RhB into leuco RhB through hydrogenation driven by electron transfer. This mechanism aligns with observations from AgNPs decorated CS–BCN matrix, where BH_4^- ions adsorb onto the CS–BCN support and transfer electrons to AgNPs, which in turn reduce nitro and dye molecules.[76,78–80]

3.5. Comparative evaluation

A comparative assessment of the catalytic performance of the novel Ag@CS–BCN nanohybrid was conducted against various conventionally supported Ag-based nanocatalysts to reduce 4-NP and organic dye molecules (MO & RhB). These results are summarised in Table 5, highlighting the superior catalytic efficacy of the Ag@CS–BCN nanohybrid. These findings underscore its significant potential and practical applicability for effectively removing hazardous organic pollutants from aqueous environments.

3.6. Cyclic stability

The reusability of the Ag@CS–BCN nanohybrid was evaluated for three model reactions: 4-NP reduction, the catalytic reduction and degradation of MO and RhB. During recyclability tests, the concentration of reactants was maintained, and only the reaction volume was altered. Therefore, the system is not ruled by mass-transport limitations. As illustrated in Fig. 9a, the catalyst retained over ~90% of its relative activity for all three pollutants even after three cycles, indicating excellent catalytic durability and reusability. This stable performance is indicative of the robust anchoring of AgNPs within the CS–BCN matrix, minimising agglomeration or leaching during consecutive runs. Fig. S2a (recycled after 4-NP reduction) displays a preserved nanosheet-like morphology, though with slight compaction compared to the fresh sample (Fig. S2b). The particle dispersion remains relatively uniform. Fig. S2b (after MO degradation) shows increased wrinkling and folding of the nanosheets, suggesting some surface restructuring due to catalytic stress, yet without major agglomeration. Fig. S2c (after RhB degradation) reveals a more compact and aggregated surface, likely due to repeated dye adsorption and reduction reactions, which may have induced mild nanoparticle sintering or polymeric rearrangement. Compared to the fresh Ag@CS–BCN nanohybrid (Fig. S2b), which shows AgNPs evenly spread on thin, layered CS–BCN sheets, the recycled Ag@CS–BCN still kept most of its original structure after use. This shows that the CS–BCN support helps hold the AgNPs in place and prevents them from clumping or breaking down, even after repeated use in tough reaction conditions.

3.7. Antimicrobial activity

In evaluating the antimicrobial abilities of the support CS–BCN matrix and the Ag@CS–BCN nanohybrid, their effects on bacterial strains, such as *S. aureus* and *E. coli*, and fungal strains, namely *C. neoformans* and *C. albicans*, were observed using the agar well diffusion method.

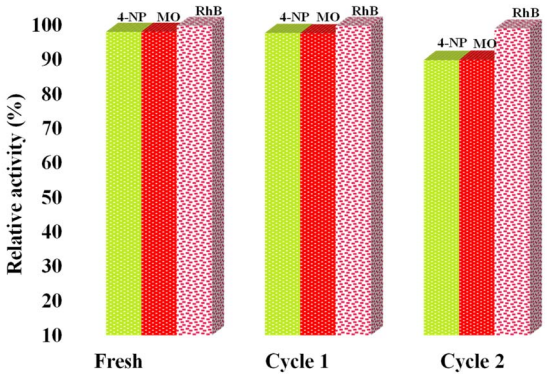

Fig. 9 Recyclability study for reducing 4-NP and degradation of MO and RhB dyes.

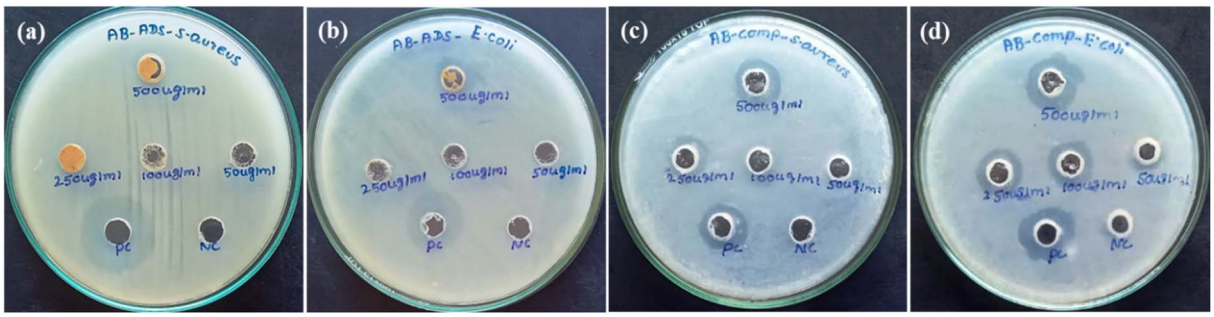

Fig. 10 (a and b) ZOI formed by support CS–BCN against major human pathogens *S. aureus* and *E. coli* at various concentrations (500, 250, 100, 50 μg mL^{-1}); (c and d) ZOI formed by Ag@CS–BCN nanohybrid against major human pathogens *S. aureus* and *E. coli* at various concentrations (500, 250, 100, 50 μg mL^{-1}); (PC) Positive Control-gentamicin; (NC) Negative Control-water.

3.7.1. Antibacterial activity. The support CS–BCN matrix demonstrated adequate antibacterial activity against *S. aureus* and *E. coli*, displaying inhibition zones of 11.1 ± 0.14 mm and 12.7 ± 0.70 mm, respectively, at a concentration of 500 μg mL^{-1}. At lower concentrations, it didn't produce any significant inhibition. The Ag@CS–BCN nanohybrid demonstrated improved antibacterial activity, resulting in larger inhibition zones of 13.25 ± 0.35 mm for *S. aureus* and 14.5 ± 0.70 mm for *E. coli* at the same 500 μg mL^{-1} concentration. Remarkably, the efficacy against *E. coli* was dose-dependent, with quantifiable inhibition even at lesser concentrations such as 250 and 100 μg mL^{-1}. As a standard, the positive control yielded inhibition zones of 18.6 ± 0.56 mm for *S. aureus* and 15.75 ± 1.06 mm for *E. coli* in the support CS–BCN assay. The key point regarding antibacterial properties is that AgNPs loading of Ag@CS–BCN nanohybrid significantly enhances the composite's ability to combat bacterial pathogens, such as *S. aureus* and *E. coli*, compared to support CS–BCN alone it's shown in Fig. 10 and Table 6. These results imply that adding silver nanoparticles to the biopolymer composite greatly improves its antibacterial activity, especially against Gram-negative bacteria.

Table 6 Standard deviation ± mean zone of inhibition (mm) obtained by CS–BCN and Ag@CS–BCN nanohybrid against *S. aureus* and *E. coli*[a]

S. no.	Name of the test sample	Name of the test organism	Zone of inhibition (mm) SD ± mean				
			500 μg mL^{-1}	250 μg mL^{-1}	100 μg mL^{-1}	50 μg mL^{-1}	PC
1	CS–BCN	*S. aureus*	11.1 ± 0.14	0	0	0	18.6 ± 0.56
		E. coli	12.7 ± 0.70	0	0	0	15.75 ± 1.06
2	Ag@CS–BCN	*S. aureus*	13.25 ± 0.35	11.5 ± 0.70	0	0	13.6 ± 0.56
		E. coli	14.5 ± 0.70	12.75 ± 0.35	12 ± 0	0	14 ± 0

[a] Significance – $p < 0.05$.

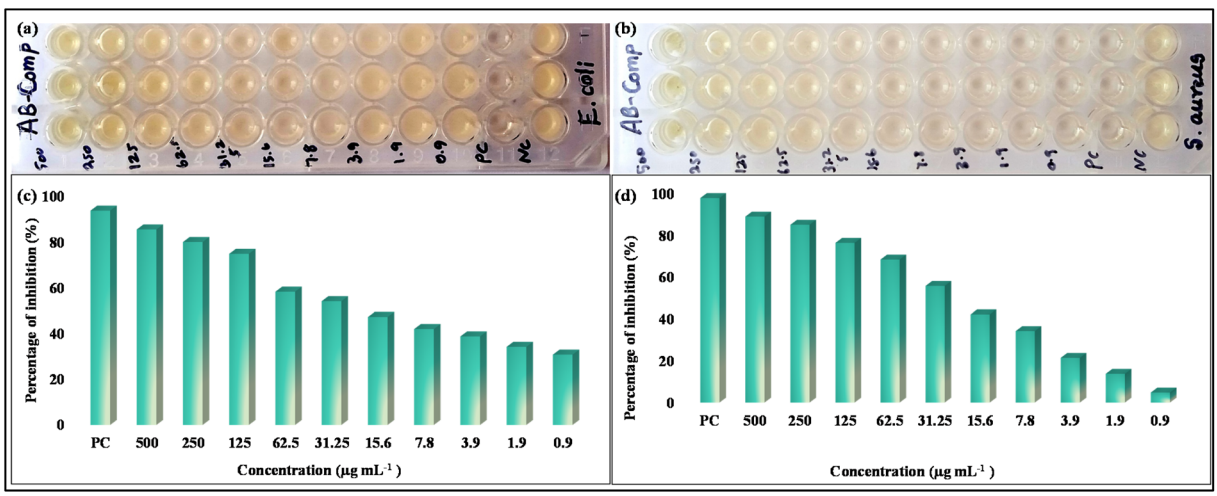

Fig. 11 Minimum inhibitory concentration (MIC) assay of the Ag@CS–BCN nanohybrid against (a and c) *E. coli* and (b and d) *S. aureus*.

3.7.2. Minimum inhibitory concentration (MIC) assay. The antibacterial efficacy of the Ag@CS–BCN nanohybrid was evaluated by determining the minimum inhibitory concentration (MIC) against both gram-positive and gram-negative strains (*E. coli* and *S. aureus*), as shown in Fig. 11 and summarised in Table 7. The MIC value, defined as the lowest concentration displaying no visible growth, was 0.9 μg mL^{-1} for both bacterial strains. The average percentage inhibition increased in a concentration-dependent manner, reaching 85.52% for *E. coli* and 89.02% for *S. aureus*, respectively, at 500 μg mL^{-1}. Dose–response analysis revealed half-maximal inhibitory concentration (IC_{50}) values of 28.30 μg mL^{-1} for *E. coli* and 12.21 μg mL^{-1} for *S. aureus*, showing good correlation with the R^2 value of 0.9798 and 0.9944, respectively. The higher sensitivity of *S. aureus* compared to *E. coli* could be ascribed to the thinner peptidoglycan layer in Gram-positive bacteria, which facilitates easier interaction with the Ag@CS–BCN nanohybrid. These results suggest that Ag@CS–BCN nanohybrid is a promising candidate for antimicrobial application.

3.7.3. Antifungal activity. The study also considered antifungal activity, with results shown in Fig. 12 and Table 8 revealed the antifungal activity of CS–BCN and Ag@CS–BCN nanohybrid, exhibiting mild inhibition of 11.1 ± 0.14 and 9.25 ± 0.35 mm against *C. neoformans* and *C. albicans* at 500 μg mL^{-1}, whereas activity declined at lower doses and demonstrated significantly enhanced antifungal properties, with zones of 17.35 ± 0.49 mm for *C. albicans* and 11.85 ± 0.49 mm for *C. neoformans* at 500 μg mL^{-1}. *C. albicans* was more susceptible than *C. neoformans*, and inhibitory effects were observed at concentrations as low as 100 μg mL^{-1} for Ag@CS–BCN nanohybrid. Amphotericin B, used as the positive control, produced inhibition zones of 11.75 ± 0.35 and 12 ± 0.70 mm for *C. neoformans* and *C. albicans*. These findings suggest that the biopolymer composite's resistance to fungus is significantly enhanced by the addition of silver nanoparticles.

Table 7 MIC and IC_{50} values of Ag@CS–BCN nanohybrid against bacterial strains

S. no.	Name of the microorganism	MIC (μg mL^{-1})	IC_{50} (μg mL^{-1})	R^2 value
1	*E. coli*	0.9	28.30	0.9798
2	*S. aureus*	0.9	12.21	0.9944

3.8. Anticancer activity

The cytotoxic effect of the prepared Ag@CS–BCN nanohybrid was evaluated *in vitro via* the MTT assay on HeLa and 3T3 cell lines displayed in Fig. 13 and 14. The assay, which quantifies mitochondrial metabolic activity as a sign of viable cells, exhibited a dose-dependent response in both cell lines following treatment with Ag@CS–BCN nanohybrid. In HeLa cells, while increasing the concentration of the synthesised Ag@CS–BCN nanohybrid (1 to 500 μg mL^{-1}), a significant reduction in viability was observed. The calculated IC_{50} value was 45.73 μg mL^{-1}, showing strong cytotoxic potential against cancer cells. At the highest concentration examined (500 μg mL^{-1}), the cell viability decreased to approximately 28.55%. The defining signs of apoptosis, such as cellular shrinkage,

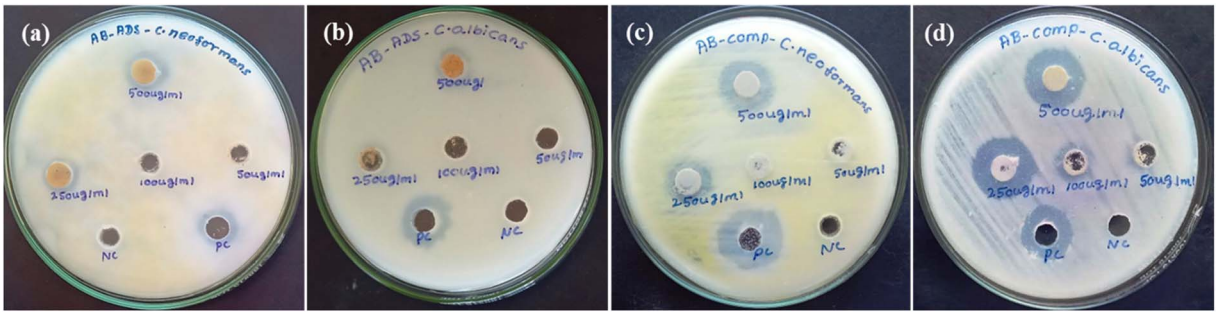

Fig. 12 (a and b) ZOI formed by support CS–BCN against the pathogenic yeast *C. neoformans* and *C. albicans* (c and d); ZOI formed by Ag@CS–BCN nanohybrid against azoles such as *C. neoformans* and *C. albicans*; (PC) Positive Control – amphotericin B; (NC) Negative Control – water.

Table 8 Standard deviation ± mean zone of inhibition (mm) obtained by CS–BCN and Ag@CS–BCN nanohybrid against *C. albicans*, *C. neoformans*[a]

S. no.	Name of the test sample	Name of the test organism	Zone of inhibition (mm) SD ± mean				
			500 μg mL^{-1}	250 μg mL^{-1}	100 μg mL^{-1}	50 μg mL^{-1}	PC
1	CS–BCN	*C. neoformans*	11.1 ± 0.14	9.75 ± 0.35	0	0	11.75 ± 0.35
		C. albicans	9.25 ± 0.35	8.35 ± 0.21	0	0	12 ± 0.70
2	Ag@CS–BCN	*C. neoformans*	11.85 ± 0.49	10.85 ± 0.91	0	0	14.6 ± 0.84
		C. albicans	17.35 ± 0.49	16.75 ± 0.35	10 ± 0	0	14.6 ± 0.56

[a] Significance – $p < 0.05$.

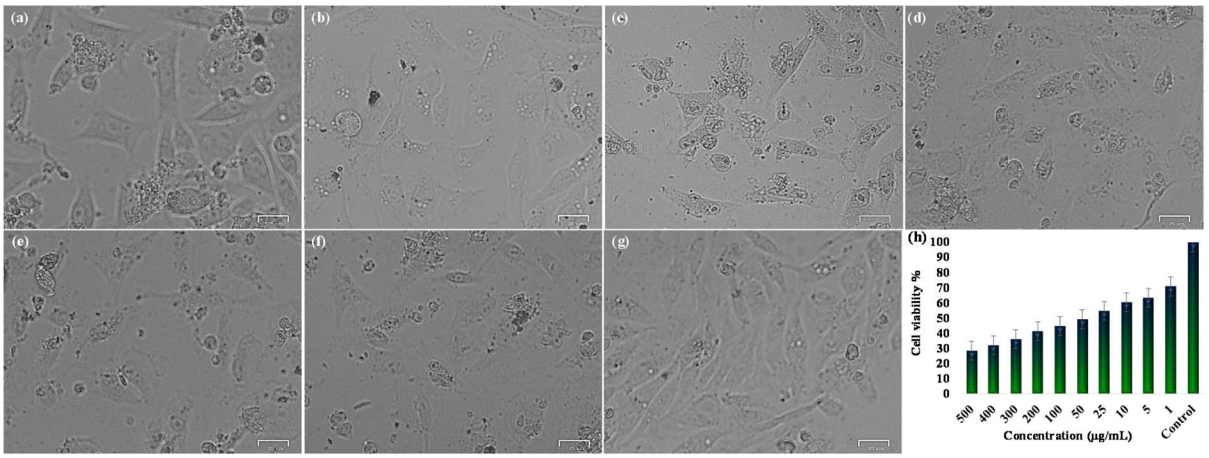

Fig. 13 Dose-dependent cytotoxicity of Ag@CS–BCN nanohybrid on HeLa cells (a) 1 μg mL^{-1}, (b) 10 μg mL^{-1}, (c) 50 μg mL^{-1}, (d) 100 μg mL^{-1}, (e) 300 μg mL^{-1}, (f) 500 μg mL^{-1}, (g) control and (h) plot for concentration *versus* cell viability%.

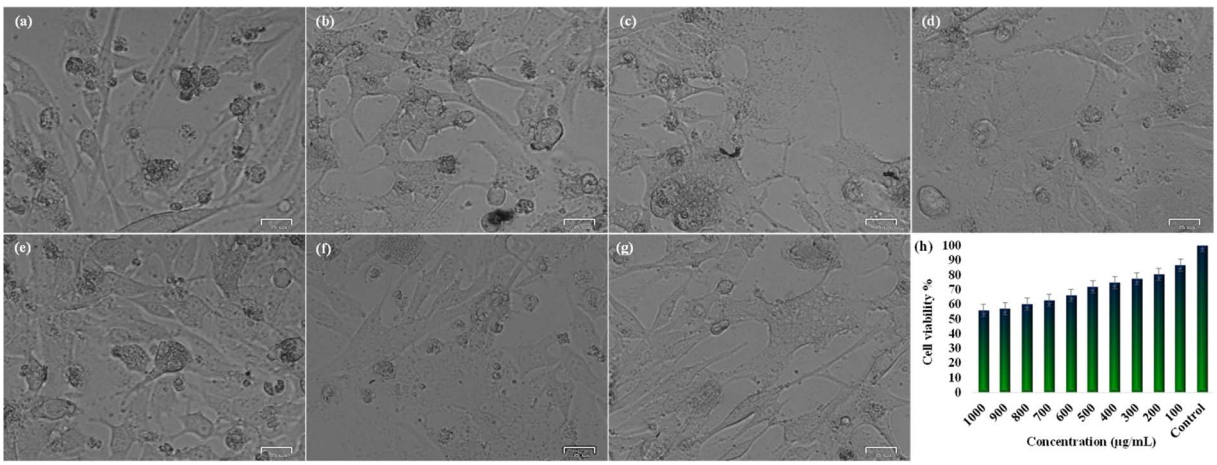

Fig. 14 Dose-dependent cytotoxicity of Ag@CS–BCN nanohybrid on 3T3 cells (a) 100 μg mL^{-1}, (b) 300 μg mL^{-1}, (c) 500 μg mL^{-1}, (d) 600 μg mL^{-1}, (e) 800 μg mL^{-1}, (f) 1000 μg mL^{-1}, (g) control and (h) plot for concentration *versus* cell viability%.

membrane blebbing, and decreased cell density, especially at concentrations over 100 μg mL^{-1}, were examined using an inverted microscope.

In contrast, Ag@CS–BCN nanohybrid showed comparatively low toxicity toward the non-cancerous 3T3 fibroblast cell line. The IC_{50} is 446.6 μg mL^{-1}, and the mean cell viability is sustained at about 55.8% even at a high dosage of 1000 μg mL^{-1}. Microscopic analysis verified that 3T3 cells maintained their adhering nature and typical spindle-shaped morphology for the entire course of treatment.

Dose–response curves were produced by nonlinear regression analysis, revealing good correlation coefficients (R^2) of 0.9672 and 0.9570 for HeLa and 3T3 cells, reinforcing the model's reliability. The selectivity of the Ag@CS–BCN nanohybrid has been demonstrated by the sharp response curve in HeLa cells compared to the gradual viability decline in 3T3 cells. The differential toxicity is further highlighted by the calculated selectivity index ($SI = IC_{50}(3T3)/IC_{50}$ (HeLa)) of ~9.8. The higher absorption and intracellular localisation of Ag@CS–BCN nanohybrid in cancer cells, which leads to increased oxidative stress, mitochondrial damage, and apoptosis induction, may be the cause of the observed selectivity. Such mechanisms, which include nuclear condensation, caspase activation, and reactive oxygen species (ROS) formation, are supported by earlier research on silver-based nanomaterials. These findings suggest more research into the apoptotic pathways and the *in vivo* effectiveness of Ag@CS–BCN nanohybrid, which may be a promising anticancer agent with minimal impact on normal cells.

4. Conclusions

In a nutshell, we have devised a novel Ag@CS–BCN nanohybrid through a multi-step process and thoroughly characterised it by various spectroscopic and microscopic analyses to study its morphology, structure, elemental composition, and stability. The prepared Ag@CS–BCN nanohybrid has confirmed its efficacy in the field of both environmental remediation and

medicinal applications. The reduction and degradation of water pollutants such as 4-NP, MO and RhB in 5, 3, and 7 min, with the conversion efficiency of 99.82%, 94.50%, and 98.89% under low-impact environmental conditions. Moreover, the Ag@CS–BCN nanohybrid, prepared *via* synthetic methods, demonstrated effective recyclability for up to three consecutive cycles, maintaining robust catalytic performance throughout for both 4-NP reduction and MO and RhB degradation reactions. Further, Ag@CS–BCN nanohybrid underwent scrutiny for antimicrobial and anticancer activities. The synthesised Ag@CS–BCN nanohybrid exhibited significant selective cytotoxicity against HeLa cancer cells ($IC_{50} = 45.73\ \mu g\ mL^{-1}$) with minimal toxicity toward normal 3T3 fibroblasts ($IC_{50} = 446.6\ \mu g\ mL^{-1}$), along with promising antimicrobial activity against selected pathogenic strains, underscoring its dual potential as an anticancer and antimicrobial agent for biomedical applications. This nanohybrid opens up opportunities for innovative approaches in both medicine and catalytic systems.

Author contributions

Aakhila Banu: conceptualisation, investigation, methodology, formal analysis, writing – original draft. C. V. Yelamaggad: resources, writing – reviewing and editing. Siddappa A. Patil: validation, resources, visualisation, supervision, formal analysis, writing – review and editing, project administration, funding acquisition.

Conflicts of interest

The authors declare that they have no known competing financial interests or personal relationships that could have appeared to influence the work reported in this paper.

Data availability

All data underpinning the findings of this study, including experimental results, are presented within the manuscript.

Supplementary information: UV-visible spectra of nitroarenes, FE-SEM images of recycled catalyst, along with schematic representations of the proposed mechanisms. See DOI: **https://doi.org/10.1039/d5ra07185b**.

Acknowledgements

Authors acknowledge Jain University (JU/MRP/CNMS/110/2025), Bangalore, India, for financial support.

References

1 M. Ismail, K. Akhtar, M. Khan, T. Kamal, M. A. Khan, A. M Asiri, J. Seo and S. B. Khan, *Curr. Pharm. Des.*, 2019, **25**, 3645–3663.
2 U. Shanker, M. Rani and V. Jassal, *Environ. Chem. Lett.*, 2017, **15**, 623–642.
3 H. Kolya and C.-W. Kang, *Toxics*, 2024, **12**, 111.
4 S. S. Emmanuel, A. A. Adesibikan, E. A. Opatola and C. O. Olawoyin, *J. Appl. Organomet. Chem.*, 2023, **37**, e7108.
5 M. Ismail, M. Khan, M. A. Khan, K. Akhtar, A. M. Asiri and S. B. Khan, *J. Appl. Organomet. Chem.*, 2019, **33**, e4971.
6 R. Jana and K. Pradhan, *Chem. Commun.*, 2024, **60**, 8806–8823.
7 H. Tokiwa, Y. Ohnishi and H. S. Rosenkranz, *Crit. Rev. Toxicol.*, 1986, **17**, 23–58.
8 P. Kovacic and R. Somanathan, *J. Appl. Toxicol.*, 2014, **34**, 810–824.
9 P. Singh, A. Mukherjee, A. Mahato, A. Pramanik and D. Dhak, *Chem. Afr.*, 2023, **6**, 561–578.
10 K. Ramamurthy, P. S. Priya, R. Murugan and J. Arockiaraj, *Environ. Sci. Pollut. Res.*, 2024, **31**, 33190–33211.
11 P. Babuji, S. Thirumalaisamy, K. Duraisamy and G. Periyasamy, *Water*, 2023, **15**, 2532.
12 A. P. Periyasamy, *Sustainability*, 2024, **16**, 495.
13 L. Xuan, Z. Ju, M. Skonieczna, P. K. Zhou and R. Huang, *MedComm*, 2023, **4**, e327.
14 B. K. Sree, N. Kumar and S. Singh, *Toxicol. Res.*, 2024, **13**, tfae077.
15 P. Patel, P. Maliekal, S. Lingayat and P. Badani, *Russ. J. Phys. Chem. B*, 2022, **16**, 869–876.
16 T. K. Das and N. C. Das, *Int. Nano Lett.*, 2022, **12**, 223–242.
17 K. A. Ryu, C. M. Kaszuba, N. B. Bissonnette, R. C. Oslund and O. O. Fadeyi, *Nat. Rev. Chem.*, 2021, **5**, 322–337.
18 A. Vaishampayan and E. Grohmann, *Microorganisms*, 2021, **10**, 61.
19 A. Haleem, A. Shafiq, S.-Q. Chen and M. Nazar, *Molecules*, 2023, **28**, 1081.
20 A. C. R. Ngo and D. Tischler, *Int. J. Environ. Res. Public Health*, 2022, **19**, 4740.
21 C. Sanchez, B. Julián, P. Belleville and M. Popall, *J. Mater. Chem. B*, 2005, **15**, 3559–3592.
22 R. Jachak, S. Chahande, J. Thaware and R. Mahakhode, in *Biogenic Sustainable Nanotechnology*, Elsevier, 2022, pp. 227–248.
23 F. Ahmad, M. M. Salem-Bekhit, F. Khan, S. Alshehri, A. Khan, M. M. Ghoneim, H.-F. Wu, E. I. Taha and I. Elbagory, *J. Nanomater.*, 2022, **12**, 1333.
24 P. Singh, S. Pandit, S. R. Balusamy, M. Madhusudanan, H. Singh, H. M. Amsath Haseef and I. Mijakovic, *Adv. Healthcare Mater.*, 2025, **14**, 2403059.
25 M. Wypij, T. Jędrzejewski, J. Trzcińska-Wencel, M. Ostrowski, M. Rai and P. Golińska, *Front. Microbiol.*, 2021, **12**, 632505.
26 N. Tripathi and M. K. Goshisht, *ACS Appl. Bio Mater.*, 2022, **5**, 1391–1463.
27 G. Rani, A. Bala, R. Ahlawat, A. Nunach and S. Chahar, *Comments Inorg. Chem.*, 2025, **45**, 1–29.
28 C.-L. Ke, F.-S. Deng, C.-Y. Chuang and C.-H. Lin, *Polymers*, 2021, **13**, 904.
29 Z. Shan, J. Huang, Y. Huang, Y. Zhou and Y. Li, *Int. J. Biol. Macromol.*, 2024, **277**, 134563.
30 Y. Kondo, T. Aoki, A. Abe and A. Tanabe, *J. Acoust. Soc. Jpn.*, 1995, **66**, 766–769.

31 B. Chandrashekharan, H. G. Sampatkumar, D. George, A. M. Antony, S. V. Doddamani, B. Sasidhar, R. G. Balakrishna and S. A. Patil, *Diamond Relat. Mater.*, 2024, **147**, 111261.
32 M. Rinaudo, *Prog. Polym. Sci.*, 2006, **31**, 603–632.
33 M. R. Kasaai, *Carbohydr. Polym.*, 2010, **79**, 801–810.
34 V. Pawariya, S. De and J. Dutta, *Carbohydr. Polym.*, 2024, **323**, 121395.
35 S. Shekhar, V. Chaudhary, B. Sharma, A. Kumar, A. K. Bhagi and K. P. Singh, *J. Polym. Environ.*, 2023, **31**, 1257–1278.
36 Z. Wang, L. Yang and W. Fang, *Journal of Chitin and Chitosan Science*, 2019, 97–144.
37 J. Chabbi, A. Aqil, N. Katir, B. Vertruyen, C. Jerôme, M. Lahcini and A. El Kadib, *Carbohydr. Polym.*, 2020, **230**, 115634.
38 L. Marin, S. Moraru, M. C. Popescu, A. Nicolescu, C. Zgardan, B. C. Simionescu and M. Barboiu, *Chem.–Eur. J.*, 2014, **20**, 4814–4821.
39 H. Tu, X. Li, K. Xie, J. Zhang, Y. Liu, X. Lin, R. Zhang and B. Duan, *Carbohydr. Polym.*, 2023, **299**, 120234.
40 A. Barth, *Biochim. Biophys. Acta, Bioenerg.*, 2007, **1767**, 1073–1101.
41 J. Kong and S. Yu, *Acta Biochim. Biophys. Sin.*, 2007, **39**, 549–559.
42 B. H. Stuart, *Infrared Spectroscopy: Fundamentals and Applications*, John Wiley & Sons, 2004.
43 J. Coates, *Encyclopedia of Analytical Chemistry*, 2000, vol. 12, pp. 10815–10837.
44 D. Lin-Vien, N. B. Colthup, W. G. Fateley and J. G. Grasselli, *The Handbook of Infrared and Raman Characteristic Frequencies of Organic Molecules*, Elsevier, 1991.
45 S. A. Thomas, J. Cherusseri, M. R. Pallavolu, D. N. Rajendran and D. Kumar, *Energy Fuels*, 2024, **38**, 13704–13721.
46 J. Xu, Y. Wang and Y. Zhu, *Langmuir*, 2013, **29**, 10566–10572.
47 Y. Zhang and M. Antonietti, *Chem.–Asian J.*, 2010, **5**, 1307–1311.
48 M. Rinaudo, *Prog. Polym. Sci.*, 2006, **31**, 603–632.
49 P. Ilgin, G. Avci, C. Silan, S. Ekici, N. Aktas, R. S. Ayyala, V. T. John and N. Sahiner, *Carbohydr. Polym.*, 2010, **82**, 997–1003.
50 C. Qin, H. Li, Q. Xiao, Y. Liu, J. Zhu and Y. Du, *Carbohydr. Polym.*, 2006, **63**, 367–374.
51 H. Djahaniani, M. Rahimi-Nasrabadi, M. Saiedpour, S. Nazarian, M. Ganjali and H. Batooli, *Int. J. Food Prop.*, 2017, **20**, 922–930.
52 N. Hlapisi, S. P. Songca and P. A. Ajibade, *MRS Adv.*, 2024, **9**, 830–836.
53 T. Gudipati, M. B. Zaman, S. Kumari, M. Sharma, P. S. Pawaiya and R. Poolla, *Mater. Sci. Semicond. Process.*, 2022, **150**, 106954.
54 W. Lei, D. Portehault, D. Liu, S. Qin and Y. Chen, *Nat. Commun.*, 2013, **4**, 1777.
55 Y. Chen, L.-Z. Cheong, J. Zhao, W. Panpipat, Z. Wang, Y. Li, C. Lu, J. Zhou and X. Su, *Int. J. Biol. Macromol.*, 2019, **123**, 261–268.
56 A. J. Kora and L. Rastogi, *Arabian J. Chem.*, 2018, **11**, 1097–1106.
57 A. M. Awwad, N. M. Salem and A. O. Abdeen, *Int. J. Ind. Chem.*, 2013, **4**, 29.
58 S. Prabhu and E. K. Poulose, *Int. Nano Lett.*, 2012, **2**, 32.
59 J. Wang, L. Shen, B. Ding, P. Nie, H. Deng, H. Dou and X. Zhang, *RSC Adv.*, 2014, **4**, 7538–7544.
60 N. Zhao, X. Fei, X. Cheng and J. Yang, *IOP Conf. Ser.:Mater. Sci. Eng.*, 2017, **242**, 012002.
61 A. Vasil'kov, T. Batsalova, B. Dzhambazov and A. Naumkin, *Surf. Interface Anal.*, 2022, **54**, 189–202.
62 H. Liu, L. Liu, Y. Du, Y. Zheng, S. Zhao and L. Yang, *Adv. Funct. Mater.*, 2025, 2420936.
63 M. Karnan, F. Oladoyinbo, G. B. Noumi, J. B. Tchatchueng, M. J. Sieliechi, M. Sathish and D. K. Pattanayak, *Electrochim. Acta*, 2020, **341**, 135999.
64 Y. Wang, J. Yu, W. Peng, J. Tian and C. Yang, *Sci. Rep.*, 2019, **9**, 5932.
65 H. G. Sampatkumar, S. Likitha, M. H. Kumar, M. Sudhanva, C. Yelamaggad, R. Dateer, K. B. Manjappa and S. A. Patil, *J. Mater. Chem. B*, 2025, **13**, 13013–13019.
66 W.-S. Wang, H. Du, R.-X. Wang, T. Wen and A.-W. Xu, *Nanoscale*, 2013, **5**, 3315–3321.
67 A. V. Rethnakumaran and M. M. Menamparambath, *Macromol. Mater. Eng.*, 2025, 2400409.
68 E. Szymańska and K. Winnicka, *Mar. Drugs*, 2015, **13**, 1819–1846.
69 V. Porchezhiyan and S. Noorjahan, *RSC Adv.*, 2016, **6**, 95564–95573.
70 S. O. Ogungbesan, E. Buxaderas, R. A. Adedokun, Y. Moglie, S. Grijalvo, M. T. García, C. Bingbing, D. Díaz Díaz and G. Fu, *ChemistrySelect*, 2024, **9**, e202404909.
71 K. S. Sing, *Pure Appl. Chem.*, 1985, **57**, 603–619.
72 N. Pradhan, A. Pal and T. Pal, *Colloids Surf., A*, 2002, **196**, 247–257.
73 A. Banu, A. M. Antony, B. Sasidhar, M. Faisal, F. A. Harraz and S. A. Patil, *Colloids Surf., A*, 2024, **697**, 134372.
74 X.-Q. Wu, X.-W. Wu, J.-S. Shen and H.-W. Zhang, *RSC Adv.*, 2014, **4**, 49287–49294.
75 W. Zhou, Y. Zhou, Y. Liang, X. Feng and H. Zhou, *RSC Adv.*, 2015, **5**, 50505–50511.
76 A. M. Antony, V. Kandathil, M. Kempasiddaiah, R. Shwetharani, R. G. Balakrishna, S. M. El-Bahy, M. M. Hessien, G. A. Mersal, M. M. Ibrahim and S. A. Patil, *Colloids Surf., A*, 2022, **647**, 129116.
77 A. M. Antony, M. R. Sonalkumari, M. I. Chamanmalik and S. A. Patil, *J. Mol. Catal.*, 2024, **564**, 114322.
78 Y. Kumar, S. Rani, J. Shabir and L. S. Kumar, *ACS Omega*, 2020, **5**, 13250–13258.
79 A. Ahmad, P. G. Roy, A. Hassan, S. Zhou, M. Azam, M. A. Z. G. Sial, A. Irfan, F. Kanwal, R. Begum and Z. H. Farooqi, *Int. J. Biol. Macromol.*, 2024, **283**, 137965.
80 S. M. Alshehri, T. Almuqati, N. Almuqati, E. Al-Farraj, N. Alhokbany and T. Ahamad, *Carbohydr. Polym.*, 2016, **151**, 135–143.

81 S. Deshmukh, R. Dhokale, H. Yadav, S. Achary and S. Delekar, *Appl. Surf. Sci.*, 2013, **273**, 676–683.
82 M. Shilpa, S. J. Shetty, S. Surabhi, J.-R. Jeong, D. V. Morales, M. Murari, V. S. Bhat, S. R. Inamdar, Ravikirana and S. Gurumurthy, *J. Mater. Sci.: Mater. Electron.*, 2024, **35**, 860.
83 V.-D. Doan, T. L. H. Nguyen, D. C. Nguyen, A.-T. Nguyen and V. T. Le, *Mol. Catal.*, 2023, **534**, 112804.
84 Y. Liu, H. Zhou, J. Wang, D. Yu, Z. Li and R. Liu, *RSC Adv.*, 2022, **12**, 3847–3855.
85 R. Selvaraj, S. A. Shetty, G. Murugesan, T. Varadavenkatesan and R. Vinayagam, *Discover Appl. Sci.*, 2025, **7**, 1–12.
86 B. Kim, W. C. Song, S. Y. Park and G. Park, *Catalysts*, 2021, **11**, 347.
87 M. Kgatle, K. Sikhwivhilu, G. Ndlovu and N. Moloto, *Catalysts*, 2021, **11**, 428.
88 B. Reddy, R. Dadigala, R. Bandi, K. Seku and A. E. Shalan, *RSC Adv.*, 2021, **11**, 5139–5148.
89 H. Veisi, S. Razeghi, P. Mohammadi and S. Hemmati, *Mater. Sci. Eng., C*, 2019, **97**, 624–631.
90 K. Naseem, M. Zia Ur Rehman, A. Ahmad, D. Dubal and T. S. AlGarni, *Coatings*, 2020, **10**, 1235.
91 W. M. Alamier, M. DY Oteef, A. M. Bakry, N. Hasan, K. S. Ismail and F. S. Awad, *ACS Omega*, 2023, **8**, 18901–18914.